

Furrow Constriction in Animal Cell Cytokinesis

Hervé Turlier,^{†*} Basile Audoly,[‡] Jacques Prost,^{†§} and Jean-François Joanny[†]

[†]Physicochimie Curie (Centre National de la Recherche Scientifique-UMR168), Institut Curie, Section de Recherche, Paris, France; [‡]Institut Jean Le Rond d'Alembert (Centre National de la Recherche Scientifique-UMR7190), Université Pierre-et-Marie-Curie, Université Paris VI, Paris, France; and [§]École Supérieure de Physique et de Chimie Industrielles de la Ville de Paris-ParisTech, Paris, France

ABSTRACT Cytokinesis is the process of physical cleavage at the end of cell division; it proceeds by ingression of an actomyosin furrow at the equator of the cell. Its failure leads to multinucleated cells and is a possible cause of tumorigenesis. Here, we calculate the full dynamics of furrow ingression and predict cytokinesis completion above a well-defined threshold of equatorial contractility. The cortical acto-myosin is identified as the main source of mechanical dissipation and active forces. Thereupon, we propose a viscous active nonlinear membrane theory of the cortex that explicitly includes actin turnover and where the active RhoA signal leads to an equatorial band of myosin overactivity. The resulting cortex deformation is calculated numerically, and reproduces well the features of cytokinesis such as cell shape and cortical flows toward the equator. Our theory gives a physical explanation of the independence of cytokinesis duration on cell size in embryos. It also predicts a critical role of turnover on the rate and success of furrow constriction. Scaling arguments allow for a simple interpretation of the numerical results and unveil the key mechanism that generates the threshold for cytokinesis completion: cytoplasmic incompressibility results in a competition between the furrow line tension and the cell poles' surface tension.

INTRODUCTION

Cytokinesis is one of the most striking hallmarks of cell division but its precise description and understanding have been challenging biologists and physicists for >50 years. Significant progress has been achieved during the last decade with advances in genomics, molecular biology, and imaging techniques, which allowed us to identify >100 proteins (1) implicated in this highly complex cellular process. Its tight regulation is as critical for cell division success as chromosome replication and separation: its failure leads generally to aberrant ploidy, which can ultimately cause cancer (2). The features and molecular processes involved in cytokinesis are remarkably similar among animal organisms (3), suggesting the existence of a common fundamental mechanism.

Mechanical engineers and physicists tried early to address the drastic cell deformation occurring during cytokinesis. Continuous elastic, viscous, analytical, and computational models of the entire cell surface have been proposed (4–8) to account for early experimental observations and force measurements performed on sea-urchin eggs (9). By contrast, most of the recent theoretical work is focused on the so-called contractile ring, based on coarse-grained descriptions (10–12) or microscopic models for motor-filament interactions (13,14). In our approach, the cell surface is viewed as a continuum, in the spirit of earlier work (4–6,8), but it is treated using recent active-gel models for acto-myosin rheology (15,16). Adhesive forces have been proposed to contribute to furrow constriction in nonanimal

Dictyostelium discoideum cells (17). Here, we consider neither cell-cell nor cell-substrate adhesion. Our model would therefore be well adapted for cell lines dividing in suspension, such as eggs or leukocytes. Recent experimental studies have highlighted that tight regulation of the contractility at the cell poles is essential for cell shape stability (18,19). Here, we show that the contractility, but also the dissipation at cell poles, are limiting factors controlling primarily the constriction of the cleavage furrow.

MODEL

The acto-myosin cortex: main source of active forces and dissipation

The cell is actively shaped by cytoskeleton elements, essentially the microtubules and the acto-myosin cortex (20). Although an intact and functional acto-myosin cortex is necessary for furrowing (21–23), it has been shown that microtubules need not be in contact with the cell surface for proper constriction (24). They therefore do not shape the cell surface directly, but are nevertheless responsible for positioning the cleavage furrow by delivering the biochemical signal that activates locally contractile forces in the cortex (25–27), as suggested by Rappaport's early experiments (28).

In animal cells, the typical plasma membrane tension is one order-of-magnitude smaller than the typical active tension developed by the acto-myosin cortex (29). In addition, the plasma membrane does not prevent cell surface expansion, because several regulatory mechanisms ensure permanent plasma membrane surface availability, including disassembly of caveolae on shorter timescales (30) and membrane trafficking on longer timescales (31,32). The mechanical role of the plasma membrane can therefore be neglected in normal conditions. It has been proposed that abrupt detachments of plasma membrane from the cortex, called blebs, can act locally as cytoplasmic pressure valves in specific cells (18,19). However, their stochastic nature at the scale of the cell still challenges efficient modeling and we therefore restrict the application of our model to nonblebbing cells such as eggs and embryos.

The cytoplasm is squeezed toward polar regions by the furrow constriction, as reported in early experiments of Hiramoto (9). It can also be

Submitted September 10, 2013, and accepted for publication November 11, 2013.

*Correspondence: herve.turlier@polytechnique.org

Editor: Jochen Guck.

© 2014 by the Biophysical Society
0006-3495/14/01/0114/10 \$2.00

<http://dx.doi.org/10.1016/j.bpj.2013.11.014>



adverted along the cortex by cortical flows. The cytoplasmic pressure associated with these flows has been measured to relax within a few seconds (33), whereas in cytokinesis, the cortical deformation occurs in several minutes. On this slower timescale, the response of the cytoplasm can therefore be captured by a uniform pressure. Viscous dissipation in the cytoplasm can be neglected, because it is generally much lower than the dissipation in the cortex, at least for cells < 1 mm in size (see the [Supporting Material](#)).

A nonlinear visco-active membrane model for the acto-myosin cortex

The response of the acto-myosin cortex is well captured by the Maxwell viscoelastic model: elastic at short timescale, viscous at longer times. Because the elastic stress is released upon renewal of the layer, the viscoelastic relaxation time of the material must be smaller than the typical time for turnover. The latter has been found to be of the order of a few tens of seconds based on fluorescence recovery after photobleaching

(FRAP) experiments in polar and equatorial cortices (34–36). This is much shorter than the typical cytokinesis duration, which is in the range of 5–30 min. The cortex can therefore be viewed as a purely viscous fluid during constriction. Inertial effects are also completely negligible (37).

Given that the cortex is thin relative to the cell radius, the cortical layer is represented by a thin shell model (38). As long as the stress tangent to the cell surface remains tensile, no buckling occurs and one can ignore the small bending moments: this is the so-called membrane theory in mechanics (39) (not to be confused with the plasma membrane). We formulate here a visco-active membrane theory of the cortex and solve it numerically for large deformations.

We use a Lagrangian description (see the [Supporting Material](#)), which makes the numerical implementation easier. The reference configuration is an initial spherical shape ([Fig. 1](#), t_0) that corresponds to the metaphase round cell (40). As suggested by observation, we assume that the cell remains axisymmetric (see [Fig. S1 A](#) and [Movie S5](#) in the [Supporting Material](#)): a section plane (e_z, e_ϕ) of the cell is shown in [Fig. 1](#). The membrane tension is therefore a diagonal tensor (see the [Supporting Material](#)) in the curvilinear frame (t, e_ϕ) ([Fig. 1](#), t_0). It involves axial and azimuthal

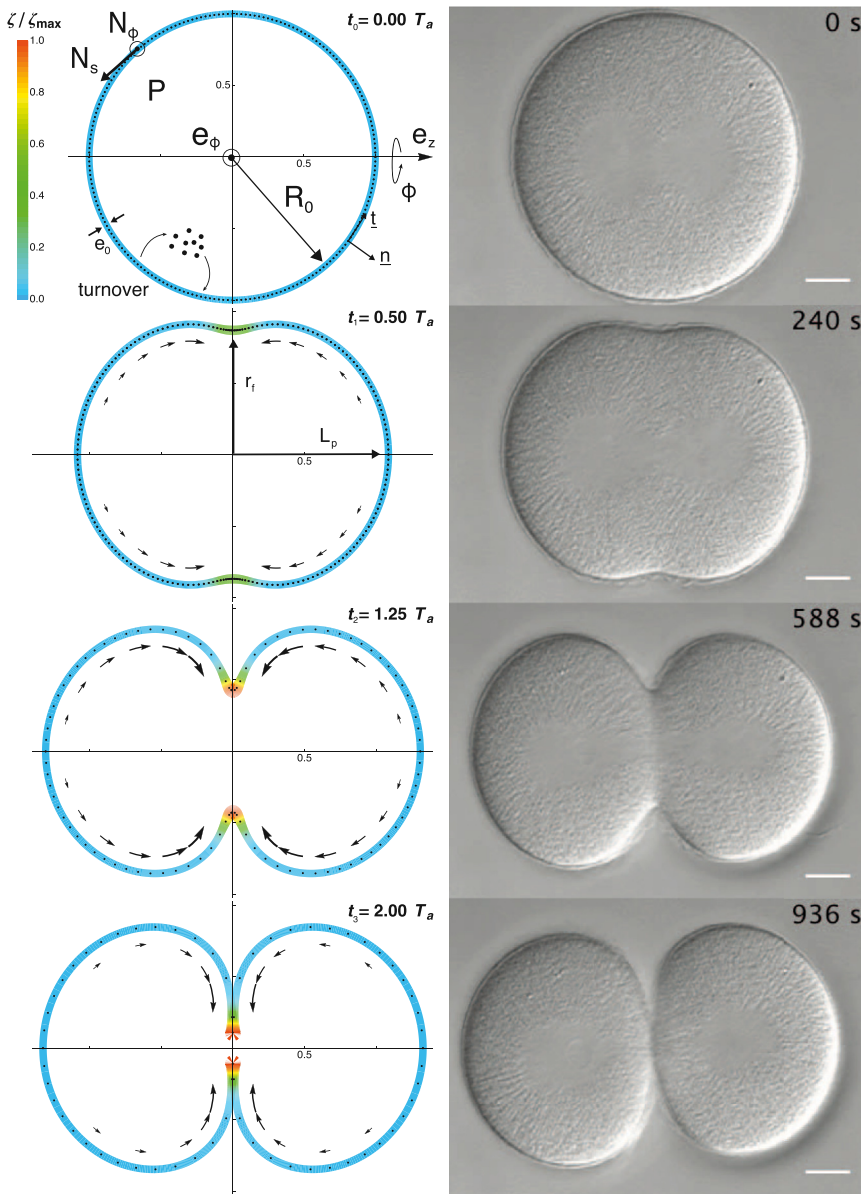


FIGURE 1 (Left) Numerical cell shape and cortex thickness evolution. (t_0) Initial spherical cortex of radius R_0 and main ingredients of the model. The membrane is axisymmetric around the axis e_z and is subjected to internal tensions N_s and N_ϕ in its axial t and azimuthal e_ϕ principal directions, and to the cytoplasmic pressure P along its normal n . The acto-myosin layer of initial thickness e_0 undergoes permanent turnover. Approximately 100 Lagrangian nodes are represented to follow the tangential membrane deformation over time (not all simulations nodes are shown). (t_1 , t_2 , and t_3) Cell cortex snapshots at successive times of constriction, in response to the rescaled myosin activity signal ζ/ζ_{\max} illustrated by the color shading. The value r_f is the furrow radius and L_p is the half pole-to-pole distance. Cortical flows along the membrane are represented by arrows of size proportional to the local tangent velocity. (Right) DIC microscopy images of a sand-dollar zygote (Dendraster) deprived of its hyaline layer and jelly coat at four equivalent times of furrow constriction. The cell is not flattened and scale bar is 20 μm . (Credits: G. Von Dassow.) To see this figure in color, go online.

components, which are denoted by N_s and N_ϕ , respectively. The membrane tension is proportional to the cortical thickness e and is the sum of a viscous and an active contribution. Viscous tensions are proportional to the viscosity η , and to the axial and azimuthal strain rates, which are defined as the symmetric part of the membrane velocity gradient and denoted, respectively, by d_s and d_ϕ . Active tensions originate from molecular motors that steadily consume free energy coming from the hydrolysis of ATP molecules to produce work. The acto-myosin layer consists of a meshwork of semi-flexible actin filaments suspended in the cytoplasmic fluid and myosin motors that bind to the filaments to exert contractile internal stresses. We use the active-gel theory of Kruse et al. (15,16) to describe the rheology of this material (see the [Supporting Material](#)). We neglect the polarity of actin filaments so that the active stress within the cortex results in an isotropic active membrane tension, proportional to the local activity $\zeta \geq 0$ of myosin motors and to the chemical free energy $\Delta\mu$ of hydrolysis of one ATP molecule. The membrane tensions finally read

$$N_s = \frac{e}{2} \zeta \Delta\mu + 2 \eta e (2 d_s + d_\phi), \quad (1a)$$

$$N_\phi = \frac{e}{2} \zeta \Delta\mu + 2 \eta e (d_s + 2 d_\phi), \quad (1b)$$

where ζ is proportional to the myosin phosphorylation, which is locally and temporally regulated by the active form of the protein RhoA (RhoA · GTP) via its effector ROCK (23,41,42). Precise measurements of the spatio-temporal localization of RhoA · GTP in several animal cells and embryos have shown an equatorial ring of active RhoA that positions the cleavage furrow (25,43): at onset of anaphase, active RhoA accumulates at the equator and forms along the acto-myosin cortex a Gaussian band of overactivity that causes cortical actin redistribution and furrowing. We mimic this active RhoA spatial zone by imposing along the membrane a Gaussian distribution of contractile overactivity $\delta\zeta^\infty$ centered at the equator,

$$\zeta(s, t) = \zeta_0 + \delta\zeta^\infty I(t) \exp\left(-\frac{1}{2}\left[\frac{s}{w}\right]^2\right), \quad (2)$$

where s is the curvilinear length from the equator along the membrane (see the [Supporting Material](#)); ζ_0 is the basal contractile activity in the membrane, responsible for cell poles' contractility; w is the signal width; $\delta\zeta^\infty$ is the amplitude of the overactivity; and $I(t)$ is a function of time varying from 0 to 1. The analysis of the RhoA · GTP signal measurements performed in Bement et al. (25) shows that the signal amplitude increases rapidly at anaphase onset and saturates over the rest of furrow ingression. Although the precise form of the function $I(t)$ may depend on the organism and conditions, we choose for Figs. 1 and 2 (and see [Movie S1](#) and [Movie S5](#)) a sigmoidal increase in time (Fig. 2, *inset*) that fits the experimental results reasonably well.

Polar actin filaments undergo permanent assembly and disassembly, preferentially polymerizing at their plus-end and depolymerizing at their minus-end. At the scale of the cortex there is therefore a permanent actomyosin turnover, measured by FRAP. Actin polymerization nucleators are located near the plasma membrane, whereas the depolymerization acts in the bulk. We describe this material dynamics by a depolymerization rate k_d within the layer thickness and a polymerization velocity v_p from the plasma membrane surface. We consider an element of cortical layer of surface a and thickness e . Incompressibility of the gel and polymerization/depolymerization processes are captured by the following Lagrangian rate of cortical volume change:

$$\frac{d(a e)}{dt} = -k_d a e + v_p a. \quad (3)$$

The stationary thickness at zero surface deformation is given by the ratio of the polymerization velocity and depolymerization rate $e_0 \equiv v_p/k_d$, as proposed in Joanny et al. (44).

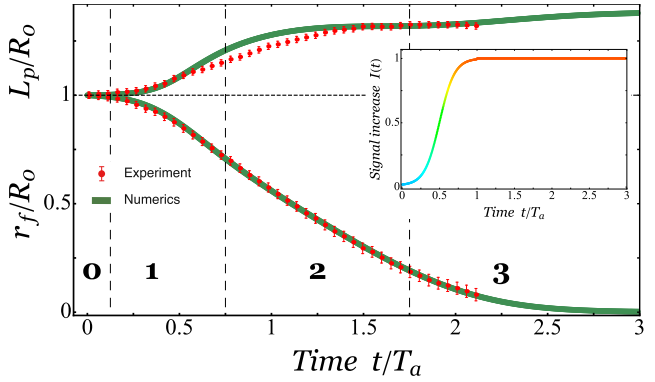


FIGURE 2 Furrow constriction dynamics. Time evolution of the furrow radius ($r_f = R_0$), and pole-to-pole half distance ($L_p = R_0$). Numerical results (line) are compared to experimental measurements of a sand-dollar zygote (points, data from the same DIC microscopy images of Fig. 1). (Vertical dashed lines) Delimiters of the four phases of constriction described in the text and numbered from 0 to 3. (*Inset*) Equatorial signal $I(t)$ applied as a function of time. To see this figure in color, go online.

Measurements show that the cytoplasmic volume is nearly conserved throughout cytokinesis (19,45). The cytoplasm is implemented here as a weakly compressible fluid with negligible viscosity. It applies therefore a uniform hydrostatic pressure onto the membrane,

$$P = -K(\mathcal{V} - \mathcal{V}_0), \quad (4)$$

where $\mathcal{V}_0 \equiv 4/3 \pi R_0^3$ is the initial cell volume. We use a value of the bulk modulus K large enough (see Table S2 in the [Supporting Material](#)) to keep the volume change $|\mathcal{V} - \mathcal{V}_0|/\mathcal{V}_0$ below 0.1% in all our simulations (see Fig. S4 A). The force balance of the membrane tensions and the cytoplasmic pressure reads

$$\operatorname{div}(N_s, N_\phi) + P \mathbf{n} = 0, \quad (5)$$

where the divergence operator depends nonlinearly on the actual configuration of the membrane. Its expression is provided in the [Supporting Material](#).

NUMERICAL RESULTS

The above equations are discretized in space by extending the method of Audoly et al. (46) to an axisymmetric geometry, as explained in the [Supporting Material](#). At every time step, the thickness and shape of the membrane are known; the unknown is the velocity field. The strain rates (d_s, d_ϕ) are expressed in terms of this velocity, and the tension is calculated by inserting the prescribed activity (Eq. 2) into Eq. 1. The balance of forces (Eq. 5) is solved for the velocity. By advecting the points of the membrane using this velocity field, we update its shape; the cortex thickness update follows from Eq. 3. To solve this set of dynamics equations (Eqs. 1–5), we adapted a preexisting C++ code (46) to the case of axisymmetric membranes. We analyzed and plotted numerical data using the software MATHEMATICA (Wolfram Alpha, <https://www.wolfram.com/mathematica/>).

In the initial state of the simulation, the membrane is a sphere with radius R_0 and uniform stationary thickness $e_0 = v_p/k_d$. It is subject to a uniform contractile activity ζ_0 . We note that the initial contractile stress ($\zeta_0 \Delta\mu/2$)

defines a typical active timescale when balanced with the viscous stress,

$$T_a \equiv \frac{2\eta}{\zeta_0 \Delta \mu}. \quad (6)$$

Typical numerical values for these parameters are picked from experimental references and summarized in [Table S1](#).

Four phases of furrow constriction

An equatorial Gaussian band of overactivity $\delta\zeta^\infty = 75$ is progressively established according to the time profile $I(t)$ plotted in [Fig. 2 \(inset\)](#). The evolution of the shape and thickness of the cell cortex is shown in [Fig. 1 \(left\)](#) (see also [Movie S1](#) and [Movie S5](#)): the four snapshots illustrate four distinct phases of constriction. The time evolution of the furrow radius r_f/R_0 and pole-to-pole distance L_p/R_0 (see definition in [Fig. 1](#)) are qualitatively different during each of the four phases, as shown in [Fig. 2](#). Numerical results are compared in [Fig. 1](#) to differential interference contrast (DIC) microscopy images of a sand-dollar zygote under cytokinesis and show very good agreement. Experimental time is rescaled by an active timescale T_a of value 468 s \approx 8 min, to successfully match experimental furrow-radius and pole-to-pole distance evolutions with numerical results in [Fig. 2](#). This timescale is perfectly consistent with the model approximations.

Phase 0: no overactivity

The initial spherical cell, shown at time $t_0 = 0$ in [Fig. 1](#), is a stable equilibrium and verifies Laplace's law $P = e_0 \zeta_0 \Delta \mu / R_0$.

Phase 1: activity increase at the equator

Following the increase of myosin activity (*inset* in [Fig. 2](#) and *color shading* in [Fig. 1](#)), the equatorial region becomes more contractile. It triggers a cortical flow toward the equator, as shown by the arrows at time $t_1 = 0.50 T_a$ in [Fig. 1](#). This actin accumulation forms an annular bundle, thereby reproducing the observed formation of the contractile ring (47). This increase in thickness (see [Fig. S2 B](#)) results from the competition between cortical flow and actin turnover. The contractile ring starts to pinch the cell, increasing the cytoplasmic pressure (see [Fig. S4 B](#)); the pole-to-pole distance increases rapidly ([Fig. 2, top](#)) and the cell adopts a prolate-like shape ([Fig. 1](#) and see [Movie S1](#) and [Movie S5](#) at time $t_1 = 0.50 T_a$), consistent with the so-called anaphase cell elongation (48).

Phase 2: plateau of activity at the equator

The amplitude of overactivity starts to saturate after a time interval of $\sim 0.75 T_a$ ([Fig. 2, inset](#)). The furrow adopts a constriction regime that is almost linear in time ([Fig. 2, bottom](#)). The pole's stretch is revealed by the increase in the gaps between the simulation nodes on snapshot $t_2 =$

$1.25 T_a$ in [Fig. 1](#). The two future daughter cells become increasingly nonspherical, especially in the furrow region (see [Movie S5](#)). There, both the deformation and the tension are strongly anisotropic (see [Fig. S3, C and D](#)), leading to widely different radii of curvature in the axial and azimuthal directions.

Phase 3: slowing down of constriction

When the furrow radius approaches zero, the pole-to-pole distance reaches a relative plateau ([Fig. 2, top](#)). The constriction starts slowing down exponentially ([Fig. 2, bottom](#)), because viscous dissipation due to the constriction of the furrow increases as its radius decreases (see [Fig. 7 D](#) later in text, and see [Fig. S5 B](#)). A significant cortical flow persists from the poles toward the equator as long as the equatorial signal is maintained (time $t_3 = 2.00 T_a$ in [Fig. 1](#)). Because this flow is balanced by turnover, the shape and surface of the polar regions no longer evolve significantly with time (see [Movie S1](#), [Movie S4](#), and [Fig. S4 C](#)). If, on the contrary, the signal at the equator is significantly decreased after cytokinesis completion, the daughter cells adopt a spherical shape (see [Movie S3](#)). This behavior is classically observed in zygotes (deprived of the external shell) when cell-cell adhesion is artificially lowered.

A threshold for complete furrow constriction

We plot in [Fig. 3 B](#) the furrow ingression as a function of time for six values of the equatorial overactivity $\delta\zeta^\infty/\zeta_0$ between 10 and 100. For $\delta\zeta^\infty/\zeta_0 > 40$, the furrow fully constricts (see *silhouetted numbers 4–6*), but slows down when the equatorial signal is decreased. For $\delta\zeta^\infty/\zeta_0 \leq 40$, the furrow radius reaches a plateau (see *silhouetted numbers 1–3*). Full constriction therefore requires that the overactivity at the equator exceeds a threshold, and the rate of constriction is dose-dependent, consistent with observations reported in Loria et al. (49). The final stationary furrow radius r_f^∞ is plotted as a function of the overactivity amplitude $\delta\zeta^\infty/\zeta_0$ in [Fig. 3 A](#). The diagram displays a saddle-node bifurcation near $\delta\zeta^\infty/\zeta_0 \approx 40$. The longer delay required to complete ingression around the threshold ([Fig. 3 B, silhouetted number 4](#)) is therefore interpreted as a critical slowing-down. Shape evolutions leading to constriction failure and completion are compared in [Movie S2 \(left, silhouetted number 2; right, silhouetted number 5\)](#).

The bifurcation diagram in [Fig. 3 A](#) reveals furthermore a noticeable hysteretic behavior, represented by the arrows. If one starts from a fully constricted state at the end of cytokinesis ($r_f \approx 0$ and $\delta\zeta^\infty/\zeta_0 > 40$) and decreases the equatorial overactivity under the threshold $\delta\zeta^\infty/\zeta_0 < 40$, the cell stays divided (unless the signal is decreased down to zero). As long as some slight equatorial tension is maintained, the divided state is therefore mechanically stable, which may prevent the furrow from regressing erroneously during the

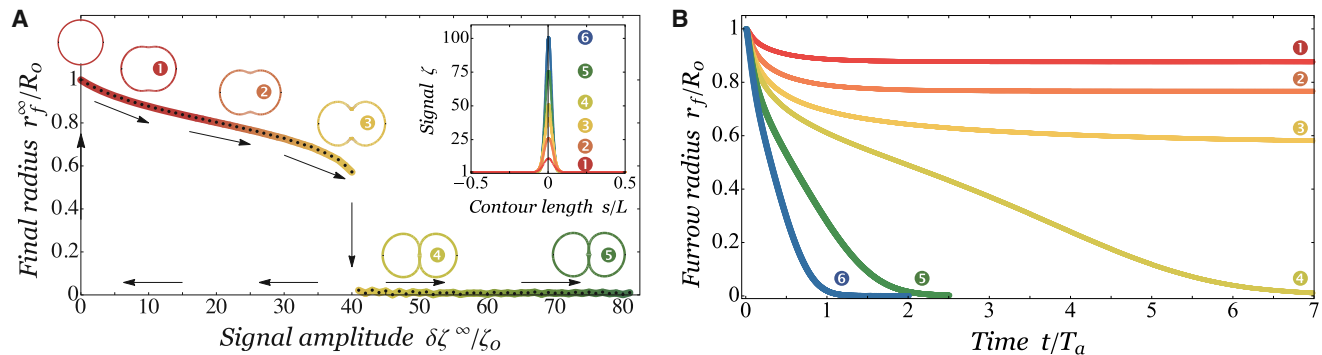


FIGURE 3 Constriction completion and failure. (A) Bifurcation diagram representing the final furrow radius r_f^∞/R_0 as a function of the amplitude of equatorial overactivity $\delta\zeta^\infty/\zeta_0$. The diagram displays a jump from constriction failure to completion for a critical amplitude $\delta\zeta^\infty/\zeta_0 \approx 40$. Final cell shapes are plotted for the six activity signals ζ , of amplitudes $\delta\zeta^\infty/\zeta_0 = 10$ (1), 25 (2), 40 (3), 50 (4), 75 (5), and 100 (6) as represented (inset) as a function of the contour length from equator s/L along the membrane (of length L). (Arrows) Hysteresis loop. Starting from a divided state above the threshold (1), for example), we decrease the equatorial signal: the cell remains divided, unless the signal is dropped down to 0—the point at which it goes back to the spherical state. (B) Furrow radius evolution r_f/R_0 as a function of time t/T_a for the six signals ζ (represented in panel A, inset). To see this figure in color, go online.

midbody formation (50). However, if the signal is decreased prematurely in the course of ingression (for $r_f/R_0 > 0.6$), the furrow regresses and cytokinesis fails, as presumably happens in Argiros et al. (51). A tight synchronization between the signaling machinery and the furrow constriction is therefore essential. The two scenarios are compared in Movie S3 with experiments.

Constriction dynamics depends on turnover

In Fig. 4 and Movie S4 we compare the constriction dynamics for three different turnover rates $k_d T_a = 30$ (circled 1), $k_d T_a = 40$ (circled 2), and $k_d T_a = 80$ (circled 3) while keeping $e_0 = v_p/k_d$ and $\delta\zeta^\infty/\zeta_0 = 75$ constant. The stationary thickness e_f^∞ in the furrow results from a competition between incoming cortical flows and turnover, and therefore decreases at higher turnover rates (Fig. 4, inset). The active tension in the furrow is proportional to the local thickness (Eq. 1) and therefore decreases at high turnover rates, which

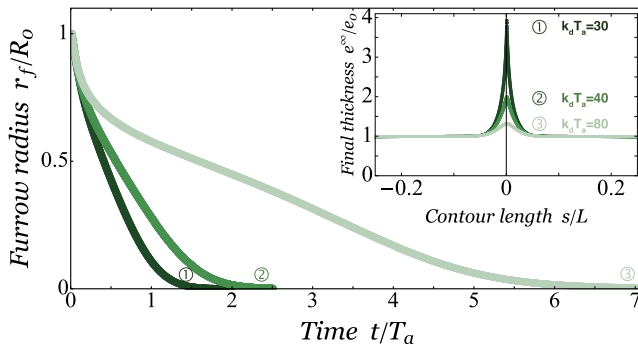


FIGURE 4 Influence of turnover on constriction. Furrow radius $r_f = R_0$ as a function of normalized time $t = T_a$ for three turnover rates: $k_d T_a = 30$ (1), $k_d T_a = 40$ (2), and $k_d T_a = 80$ (3). (Inset) Corresponding steady-state membrane thickness $e_1 = e_0$ along the rescaled contour length $s = L$ from equator (L is the total membrane midline length). To see this figure in color, go online.

lowers the rate of furrow ingression as shown on Fig. 4. We expect a large increase of turnover to impair the completion of the furrow ingression if the equatorial signal is close to the constriction threshold. Actin turnover is therefore a critical variable for cytokinesis completion; it has to be tightly regulated by the cell directly via depolymerization and polymerization and indirectly via active cortical flows.

Cytokinesis duration is independent of initial cell size

The duration of cytokinesis has been recently reported to be independent of cell initial size in *Caenorhabditis elegans* embryos (52). This remarkable property ensures the tight synchronization of daughter cells development during embryogenesis. We performed numerical constrictions with various initial cell size radii R_0 between 0.5 and 4. Measurements performed on embryos of several organisms (25) revealed the existence of a linear relationship between the initial cell size R_0 and the width w of the Gaussian RhoA-GTP zone: we thus choose w proportionally to R_0 , keeping all the other parameters constant (see Table S1). The evolution of the furrow radius with time is plotted in Fig. 5 for four different values of R_0 and w . We observe that the duration of furrow constriction is independent of R_0 provided that $w \propto R_0$. Our model reproduces this robust feature of cytokinesis.

SCALING MODEL

The numerical results can be interpreted in terms of scaling arguments based on a minimal geometry sketched in Fig. 6 A, that was proposed in 1972 by Yoneda and Dan (53). The cell poles are represented by two portions of sphere of radius R under constant active tension $N^a_0 = e_0 \zeta_0 \Delta \mu/2$ and are connected by a ring of radius r_f and width w . The contractile ring is submitted to an active line

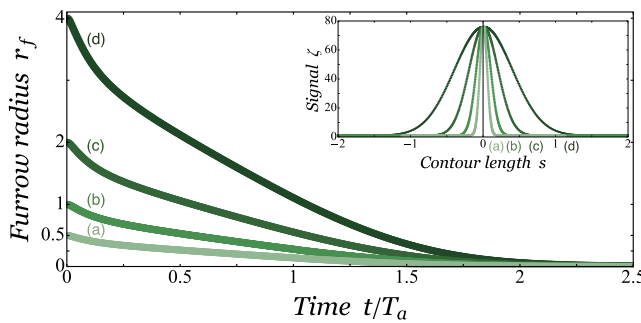


FIGURE 5 Cytokinesis duration is independent of initial cell size. Furrow radius r_f as a function of time $t = T_a$ for four initial cell radii $R_0 = 0.5, 1, 2$, and 4. (Inset) Corresponding Gaussian activity signals of width w proportional to R_0 , plotted as a function of the membrane midline contour length s . To see this figure in color, go online.

tension $\gamma \approx w(N_f^a - N_0^a)$, where N_f^a is the mean contractile surface tension in the furrow. The competition with cortical tension at cell poles is measured by the dimensionless parameter

$$\kappa = \frac{\gamma}{2R_0N_0^a} \approx \frac{w}{2R_0} \left(N_f^a - N_0^a \right) / N_0^a.$$

The opening angle θ defined in Fig. 6 A is a measure of the constriction state of the cell.

Cytokinesis completion is controlled by the difference of contractility between the contractile ring and the poles

The polar contractility tends to reduce the surface $A_p = 4\pi R^2(1 + \cos\theta)$ of the cell poles, whereas the line tension tends to reduce the contractile ring circumference $r_f = R\sin\theta$. These effects are captured by a simple mechanical energy $\varepsilon = 2\pi r_f \gamma + 2A_p N^a_0$. Cytoplasmic volume conservation can be written as $R_0 = R(\theta)^{1/3}$, where $F(\theta)$ is a smooth function of θ defined in the Supporting Material. The mechanical energy, rescaled by $\varepsilon_0 = 4\pi R_0^2 N^a_0$ for a spherical cell, depends only on κ and θ and reads

$$\frac{\varepsilon}{\varepsilon_0} = \frac{\kappa \sin \theta}{F(\theta)^{1/3}} + \frac{1 + \cos \theta}{F(\theta)^{2/3}}. \quad (7)$$

We plotted in Fig. 6 B the mechanical energy $\varepsilon/\varepsilon_0$ as a function of θ for various values of κ . The minima of $\varepsilon/\varepsilon_0$ are the local equilibrium states of the cell. Starting from a spherical cell at $\theta = \pi/2$, the final shape is reached at the first local minimum of energy. For $\kappa = 0$ (red curve), in absence of any contractile ring, the spherical cell $\theta = \pi/2$ is the minimum of energy. As the control parameter κ increases, i.e., the contractile ring line tension increases, the first local minimum of ε shifts toward a more constricted state ($\theta = \pi/2$), but the constriction is still incomplete. For $\kappa \geq 0.4$, the local minimum disappears at the benefit of a single global minimum, corresponding to the fully constricted state $\theta = 0$

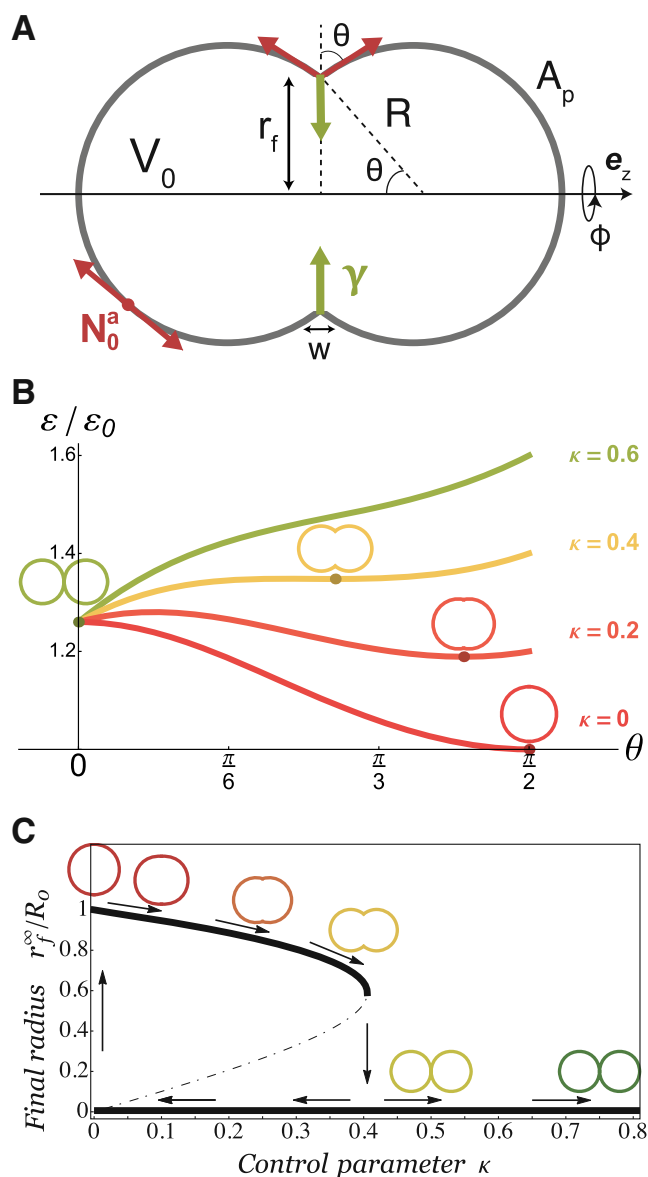


FIGURE 6 Scaling model. (A) Sketch of the minimal geometry proposed by Yoneda and Dan (53): Two portions of sphere of surface A_p and surface tension N^a_0 are pinched by an equatorial ring of radius r_f , of width w , and of line tension γ . The opening angle θ characterizes the constriction state of the cell and the cytoplasmic volume-enclosed V_0 is conserved. (B) Mechanical energy profile $E = E_0$ as a function of the constriction state θ for four values of $\kappa = \gamma/2R_0N^a_0$. Local minima of the energy correspond to equilibrium states (darker points), above which are plotted the corresponding cell shapes. (C) Bifurcation diagram representing the final furrow radius $r_f^\infty = R_0$ as a function of the control parameter κ . The upper branch and the branch $r_f = 0$ are stable branches, but one branch (dot-dashed) is unstable. The critical point is a saddle-node, and the bifurcation classically exhibits an hysteresis (see arrows). Final cell shapes, starting from a spherical cell, are plotted for the six following values of the control parameter: $\kappa = 0, 0.1, 0.25, 0.4, 0.5$, and 0.75. To see this figure in color, go online.

(green curve): constriction succeeds. This simple energetic approach of the constriction completion uncovers the fundamental mechanism of cytokinesis: cell-volume conservation enforces a competition between the line tension of the ring

(which tends to minimize its circumference) and the contractility of the poles (which resists the associated cell-surface increase).

This competition drives a first-order transition from cytokinesis failure to constriction completion. We plot alternately in Fig. 6 C the bifurcation diagram of the final constriction state r_f^∞ (corresponding to the first minimum of energy in Fig. 6 B) as a function of the control parameter κ . Similarly to the numerical results (Fig. 3 A), scaling arguments reveal a jump from partial to complete constriction above a critical threshold of the difference of contractility between the furrow and the poles, of value $\kappa \approx 0.4$ (see the Supporting Material). The energy plot in Fig. 6 B shows clearly that $\theta = 0$ is a possible local energy minimum for $\kappa > 0$, and therefore that the divided state is mechanically stable, which clarifies the origin of the hysteresis behavior, illustrated by arrows on Fig. 6 C.

The contractility difference between the contractile ring and poles also controls the dynamics of constriction

The mechanical power of active effects (Eq. 7) is exactly dissipated by viscous cell deformations (see numerical results in Fig. S5 A). The viscous dissipation is made of two contributions, the stretching of the poles and the constriction of the ring, which we estimate in scaling. The volume of acto-myosin in the poles is $V_p = 2A_p e_p$ and in the ring $V_f = 2\pi r_f w e_f$, where w and e_f are the width and thickness of the contractile ring. According to the numerical results (see Fig. S2 D), the thickness of the actin layer at poles does not vary appreciably. The value $e_p \approx e_0$ and the ring thickness e_f reach a steady-state value that depends on turnover. This yields the viscous dissipated power

$$\mathcal{P}_d = \frac{1}{2} \eta \left[V_p \left(\frac{1}{R} \frac{dr_f}{dt} \right)^2 + V_f \left(\frac{1}{r_f} \frac{dr_f}{dt} \right)^2 \right]. \quad (8)$$

From the balance of mechanical and dissipated powers $dE/dt + \mathcal{P}_d = 0$, we calculate the rate of furrow constriction as a positive function \mathcal{H} of θ , κ , and λ only (see the Supporting Material)

$$T_a \frac{dr_f}{dt} = -R_0 \mathcal{H}(\theta, \kappa, \lambda), \quad \text{with } \lambda \equiv \frac{e_f}{e_0} \frac{w}{2R_0}. \quad (9)$$

From Eq. 9, we can solve for the furrow radius r_f as a function of time and conclude that

1. The constriction timescale is set by $T_a = \eta e_0 / N^a_0$, as defined in Eq. 6, which measures the typical active time of viscous stretching of the poles.
2. The values κ and λ control the rate of constriction, and

$$\kappa \approx \frac{w}{2R_0} \left(\frac{\zeta_f e_f}{\zeta_0 e_0} - 1 \right)$$

characterizes the dependence of the constriction rate on the contractility difference between the ring and the poles, and depends on the normalized furrow activity ζ_f/ζ_0 and on turnover via the normalized thickness e_f/e_0 . The value λ depends essentially on turnover via e_f . We plot in Fig. 7 A the furrow radius r_f evolution as a function of time for various values of κ between 0.1 and 1, at fixed $\lambda = 0.1$, and recover qualitatively the same dynamics as in the numerical results. In Fig. 7 B we keep ζ_f/ζ_0 constant and plot r_f as a function of time t/T_a for four values of e_f/e_0 between 1 and 4, thereby mimicking the competition between cortical flows and actin turnover. Again we retrieve qualitatively the same behavior as for the continuous model: decreasing the furrow thickness e_f , thereby enhancing turnover, slows down the constriction and can even impede its completion (see curve $e_f/e_0 = 1$).

3. If we assume that w scales linearly with R_0 , then we find that κ and λ , which are both proportional to w/R_0 , become independent of the initial cell radius and so does \mathcal{H} . The constriction rate in Eq. 9 is proportional to the initial radius, and the cytokinesis duration becomes independent of initial cell size, as illustrated on Fig. 7 C, which reproduces the numerical results of Fig. 5.

We show that the dissipation associated to the poles stretching participates largely to the slowing-down of furrow constriction, consistently with numerical results (see Fig. S5 B): the decrease of r_f is indeed much more rapid in Fig. 7 D for vanishing poles dissipation ($V_p \rightarrow 0$ in Eq. 8). These results suggest that the contractility and the viscosity of the polar cortex are both critical parameters to consider in accounting for the dynamics of furrow constriction. In the limiting case of an isolated visco-active ring (no poles at all), scaling arguments yield a purely exponential constriction dynamics (dashed line in Fig. 7 D), consistent with experimental contraction of isolated rings in vitro (54). We can retrieve this scaling by a simple balance of viscous forces $\eta w e_f / r_f dr_f/dt$ with the constricting force $\gamma = w N^a_f = w e_f \zeta_f \Delta \mu$ in the ring, which leads immediately to $r_f/R_0 = e^{-\tau t}$, with $\tau = 2\eta/\zeta_f \Delta \mu$ the characteristic active timescale of the problem. The constriction dynamics of an isolated visco-active ring depends, therefore, strongly on the ratio of myosin activity ζ_f and acto-myosin viscosity η (controlled by cross-linking) but becomes independent of actin turnover, consistent with recent experimental results (55).

DISCUSSION

Using both numerical and scaling analyses, we rationalize the physical mechanisms governing ring constriction in the cytokinesis of animal cells. Following the seminal work of White and Borisy (6) and Bray and White (56), we show that a gradient of surface contractility from the poles to the

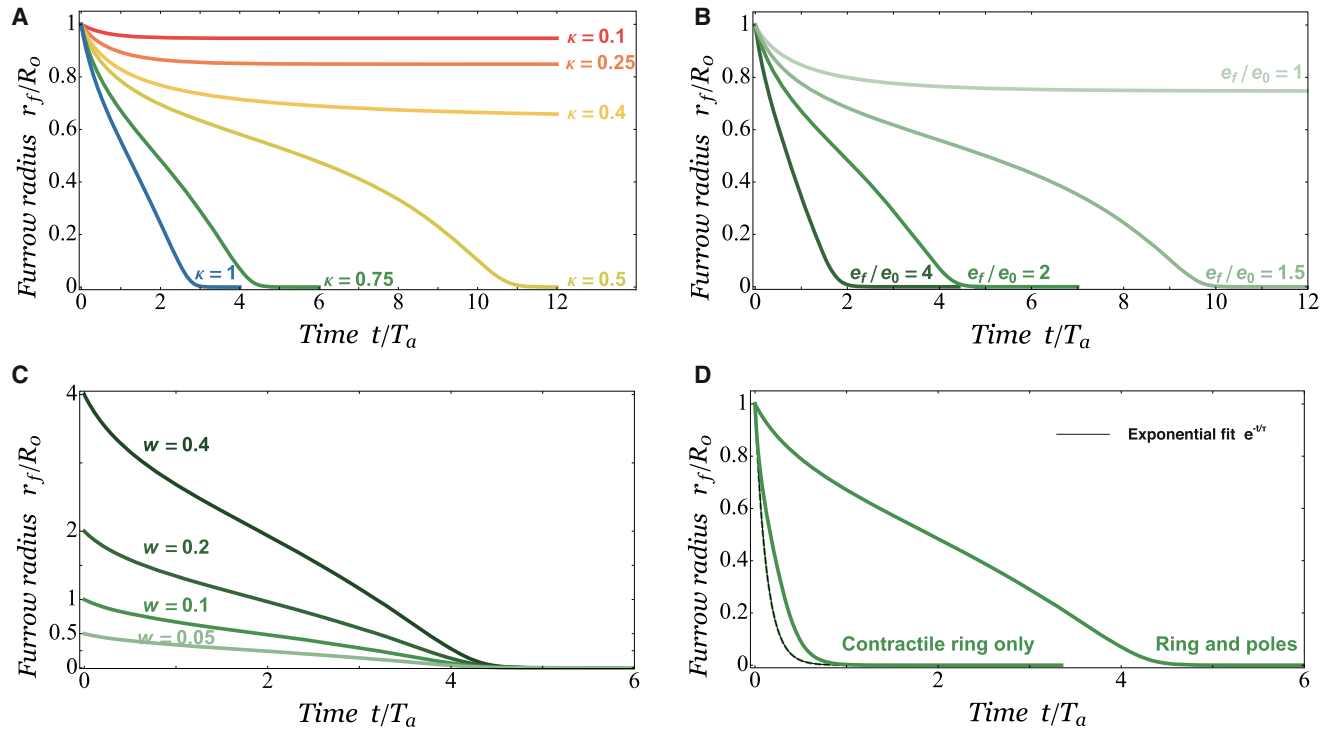


FIGURE 7 Constriction dynamics in scaling. Normalized furrow radius evolution $r_f = R_0$ with time $t = T_a$. (A) For $\kappa = 0.1, 0.25, 0.4, 0.5, 0.75$, and 1 , with constant $\lambda = 0.1$. For $\kappa \lesssim 0.4$, the furrow radius reaches a plateau indicating constriction failure, whereas for $\kappa \gtrsim 0.4$ constriction is complete and its speed increases with κ . (B) For $e_f = e_0$ between 1 and 4 , keeping $\zeta_f/\zeta_0 = 8$ and $w = R_0 = 0.1$ constant. Constriction slows down when $e_f = e_0$ decreases from 4 to 1.5 , and can even fail when it drops to 1 . (C) For four initial cell radii $R_0 = 0.5, 1, 2$, and 4 , where the ring width w is increased proportionally, $w = 0.05, 0.1, 0.2$, and 0.4 . The values $e_f = e_0 = 2$ and $\zeta_f/\zeta_0 = 8$ are maintained constant. The rate of constriction increases proportionally to the ring width, leading to the same constriction duration for the four cell sizes. (D) For a cell with dissipation due to the ring constriction only and with dissipation due to poles stretching and ring constriction ($\zeta_f/\zeta_0 = 8$, $e_f = e_0 = 2$, $w = R_0 = 0.1$). (Dashed line) Constriction of an isolated ring (no poles) fitted with the exponential function $e^{-t/\tau}$ with $\tau = 2\eta/\zeta_f \Delta\mu$. To see this figure in color, go online.

equator is sufficient to drive cytokinesis and to reproduce its main features: formation of the contractile ring, cortical flow toward the equator, and furrow constriction. Starting from a quite fundamental physical model of the cortex—a thin viscous layer producing active contraction and subjected to a uniform cytoplasmic pressure—we are able to reproduce realistic shapes of dividing embryos. We provide quantitative criteria for cytokinesis completion and propose a general framework for interpreting and characterizing constriction failure. We furthermore demonstrate the physical mechanism leading to the independence of cytokinesis duration on the initial cell size in embryos (52), and we highlight the critical influence of actin turnover.

A scaling model is then proposed to interpret the numerical results. It explains and successfully reproduces the properties of furrow constriction, despite its simplified geometry. It notably demonstrates that the contractility difference between the poles and the furrow is the key parameter for both cytokinesis completion and constriction dynamics. This highlights a critical role of the polar cortex in cytokinesis success and dynamics.

We reproduce accurately the experimental constriction dynamics and shape evolution of a sand-dollar embryo. Pre-

cise spatio-temporal measurements of RhoA-GTP along the cortex over the entire time of constriction would, however, be required for our simulation to reproduce an experiment in full detail. Estimates of cortex turnover are also required to account for the accumulation of actin in the ring via cortical flows, which can play a major role in constriction dynamics. FRAP measurements of the cortex provide reasonable values for the turnover timescale (36), but we have neglected here the possible nonuniformity of turnover along the cortex for the sake of simplicity. RhoA-GTP is indeed known for also promoting actin polymerization via the formin mDia1 (23), and the ring formation is, then, likely to be the result of accumulation by cortical flows and higher polymerization (34,35). In contrast to this, myosin activity, promoted by RhoA-GTP via its effector ROCK, has been shown to enhance actin filament disassembly both in vitro and in vivo (34,57). Altogether, the local activation of RhoA is likely to enhance nonuniform turnover. A more rigorous implementation of nonuniform turnover would require substantial progress in the theoretical understanding and quantitative characterization of in vivo disassembly of actin by myosin motors, which is far beyond this study. We argue nevertheless that the

fundamental trends highlighted in our study will remain valid. Based on quantitative studies in *C. elegans* (58), our model assumed that the frictional loss associated with cortex sliding along the plasma membrane and cytosol was negligible compared to viscous dissipation associated with cortex deformation. It would, however, be interesting to evaluate the effect of friction on the constriction dynamics in a further development of the model.

Our model demonstrates that the equatorial contractile region does not need to be structurally different from the rest of the cortex, but only more contractile. The actin filament orientation may, however, be anisotropic in the membrane plane, in particular in the furrow region (59), because their spatial organization is expected to be dynamically coupled to cortical flows (15,16). We expect that our results will not be changed qualitatively if the flow alignment effects are taken into account, but we can conjecture that the alignment of actin filaments in the furrow (7,38) lowers the activity threshold for full constriction.

Finally, we would expect the threshold value to drop rapidly, or even to vanish, if the constraint of cytoplasm incompressibility is partially relaxed (as would happen, for instance, by the release of cytoplasmic fluid through membrane pores). Conversely, constriction success may be impaired by a significant increase of cytoplasmic bulk viscoelasticity (60). Variability among animal species and among differentiated cells in an otherwise same organism may thus be revealed by different strategies for ensuring constriction success. These subtle physical effects suggest future lines for experimental investigations and potential improvements of our description and understanding of furrow constriction in animal cell cytokinesis.

SUPPORTING MATERIAL

Continuous Model, Discrete Formulation, Numerical Implementation, Scaling Model, two tables, six figures, 58 equations, five movies and references (61–70) are available at [http://www.biophysj.org/biophysj/supplemental/S0006-3495\(13\)01244-7](http://www.biophysj.org/biophysj/supplemental/S0006-3495(13)01244-7).

The authors are very grateful to G. Von Dassow and C. B. Shuster for providing experimental videos of dividing embryos and thank M. Piel and C. Roubinet for helpful comments on the manuscript.

This work was supported by the European network MitoSys project.

REFERENCES

- Eggert, U. S., T. J. Mitchison, and C. M. Field. 2006. Animal cytokinesis: from parts list to mechanisms. *Annu. Rev. Biochem.* 75:543–566.
- Fujiwara, T., M. Bandi, ..., D. Pellman. 2005. Cytokinesis failure generating tetraploids promotes tumorigenesis in p53-null cells. *Nature*. 437:1043–1047.
- Green, R. A., E. Paluch, and K. Oegema. 2012. Cytokinesis in animal cells. *Annu. Rev. Cell Dev. Biol.* 28:29–58.
- Greenspan, H. P. 1978. On fluid-mechanical simulations of cell division and movement. *J. Theor. Biol.* 70:125–134.
- Akkas, N. 1980. On the biomechanics of cytokinesis in animal cells. *J. Biomech.* 13:977–988.
- White, J. G., and G. G. Borisy. 1983. On the mechanisms of cytokinesis in animal cells. *J. Theor. Biol.* 101:289–316.
- Zinemanas, D., and A. Nir. 1987. On the viscous deformation of biological cells under anisotropic surface tension. *J. Fluid Mech.* 193:217–241.
- He, X., and M. Dembo. 1997. On the mechanics of the first cleavage division of the sea urchin egg. *Exp. Cell Res.* 233:252–273.
- Hiramoto, Y. 1971. A photographic analysis of protoplasmic movement during cleavage in the sea urchin egg. *Dev. Growth Differ.* 13:191–200.
- Zhang, W., and D. N. Robinson. 2005. Balance of actively generated contractile and resistive forces controls cytokinesis dynamics. *Proc. Natl. Acad. Sci. USA*. 102:7186–7191.
- Zumdieck, A., M. Cosentino Lagomarsino, ..., F. Jülicher. 2005. Continuum description of the cytoskeleton: ring formation in the cell cortex. *Phys. Rev. Lett.* 95:258103.
- Srivastava, P., R. Shlomovitz, ..., M. Rao. 2013. Patterning of polar active filaments on a tense cylindrical membrane. *Phys. Rev. Lett.* 110:168104.
- Zumdieck, A., K. Kruse, ..., F. Jülicher. 2007. Stress generation and filament turnover during actin ring constriction. *PLoS ONE*. 2:e696.
- Mendes Pinto, I., B. Rubinstein, ..., R. Li. 2012. Actin depolymerization drives acto-myosin ring contraction during budding yeast cytokinesis. *Dev. Cell*. 22:1247–1260.
- Kruse, K., J.-F. Joanny, ..., K. Sekimoto. 2005. Generic theory of active polar gels: a paradigm for cytoskeletal dynamics. *Eur. Phys. J. E Soft Matter*. 16:5–16.
- Marchetti, M. C., J.-F. Joanny, ..., R. A. Simha. 2013. Hydrodynamics of soft active matter. *Rev. Mod. Phys.* 85:1143.
- Poirier, C. C., W. P. Ng, ..., P. A. Iglesias. 2012. Deconvolution of the cellular force-generating subsystems that govern cytokinesis furrow ingression. *PLOS Comput. Biol.* 8:e1002467.
- Rankin, K. E., and L. Wordeman. 2010. Long astral microtubules uncouple mitotic spindles from the cytokinetic furrow. *J. Cell Biol.* 190:35–43.
- Sedzinski, J., M. Biro, ..., E. Paluch. 2011. Polar acto-myosin contractility destabilizes the position of the cytokinetic furrow. *Nature*. 476:462–466.
- Fletcher, D. A., and R. D. Mullins. 2010. Cell mechanics and the cytoskeleton. *Nature*. 463:485–492.
- Mabuchi, I., and M. Okuno. 1977. The effect of myosin antibody on the division of starfish blastomeres. *J. Cell Biol.* 74:251–263.
- Straight, A. F., A. Cheung, ..., T. J. Mitchison. 2003. Dissecting temporal and spatial control of cytokinesis with a myosin II inhibitor. *Science*. 299:1743–1747.
- Dean, S. O., S. L. Rogers, ..., J. A. Spudich. 2005. Distinct pathways control recruitment and maintenance of myosin II at the cleavage furrow during cytokinesis. *Proc. Natl. Acad. Sci. USA*. 102:13473–13478.
- von Dassow, G., K. J. C. Verbrugge, ..., W. M. Bement. 2009. Action at a distance during cytokinesis. *J. Cell Biol.* 187:831–845.
- Bement, W. M., H. A. Benink, and G. von Dassow. 2005. A microtubule-dependent zone of active RhoA during cleavage plane specification. *J. Cell Biol.* 170:91–101.
- Su, K.-C., T. Takaki, and M. Petronczki. 2011. Targeting of the RhoGEF Ect2 to the equatorial membrane controls cleavage furrow formation during cytokinesis. *Dev. Cell*. 21:1104–1115.
- Atilgan, E., D. Burgess, and F. Chang. 2012. Localization of cytokinesis factors to the future cell division site by microtubule-dependent transport. *Cytoskeleton (Hoboken)*. 69:973–982.
- Rappaport, R. 1996. Cytokinesis in Animal Cells. Cambridge University Press, Cambridge, UK.
- Tinevez, J. Y., U. Schulze, ..., E. Paluch. 2009. Role of cortical tension in bleb growth. *Proc. Natl. Acad. Sci. USA*. 106:18581–18586.

30. Sinha, B., D. Köster, ..., P. Nassoy. 2011. Cells respond to mechanical stress by rapid disassembly of caveolae. *Cell.* 144:402–413.
31. Albertson, R., B. Riggs, and W. Sullivan. 2005. Membrane traffic: a driving force in cytokinesis. *Trends Cell Biol.* 15:92–101.
32. Dyer, N., E. Rebollo, ..., M. González-Gaitán. 2007. Spermatocyte cytokinesis requires rapid membrane addition mediated by ARF6 on central spindle recycling endosomes. *Development.* 134:4437–4447.
33. Charras, G. T., J. C. Yarrow, ..., T. J. Mitchison. 2005. Non-equilibration of hydrostatic pressure in blebbing cells. *Nature.* 435:365–369.
34. Guha, M., M. Zhou, and Y. L. Wang. 2005. Cortical actin turnover during cytokinesis requires myosin II. *Curr. Biol.* 15:732–736.
35. Murthy, K., and P. Wadsworth. 2005. Myosin-II-dependent localization and dynamics of F-actin during cytokinesis. *Curr. Biol.* 15:724–731.
36. Fritzsche, M., A. Lewalle, ..., G. T. Charras. 2013. Analysis of turnover dynamics of the submembranous actin cortex. *Mol. Biol. Cell.* 24:757–767.
37. Batchelor, G. K. 1967. An Introduction to Fluid Dynamics. Cambridge University Press, Cambridge, UK.
38. Salbreux, G., J. Prost, and J.-F. Joanny. 2009. Hydrodynamics of cellular cortical flows and the formation of contractile rings. *Phys. Rev. Lett.* 103:058102.
39. Green, A. E., and W. Zerna. 2002. Theoretical Elasticity. Dover Publications, Mineola, NY, pp. 386–389.
40. Maddox, A. S., and K. Burridge. 2003. RhoA is required for cortical retraction and rigidity during mitotic cell rounding. *J. Cell Biol.* 160:255–265.
41. Kimura, K., M. Ito, ..., K. Kaibuchi. 1996. Regulation of myosin phosphatase by Rho and Rho-associated kinase (Rho-kinase). *Science.* 273:245–248.
42. Uehara, R., G. Goshima, ..., E. R. Griffis. 2010. Determinants of myosin II cortical localization during cytokinesis. *Curr. Biol.* 20: 1080–1085.
43. Yoshizaki, H., Y. Ohba, ..., M. Matsuda. 2003. Activity of Rho-family GTPases during cell division as visualized with FRET-based probes. *J. Cell Biol.* 162:223–232.
44. Joanny, J. F., K. Kruse, ..., S. Ramaswamy. 2013. The actin cortex as an active wetting layer. *Eur. Phys. J. E Soft Matter.* 36:52–58.
45. Hiramoto, Y. 1958. A quantitative analysis of protoplasmic movement during cleavage in the sea urchin egg. *J. Exp. Biol.* 35:407–424.
46. Audoly, B., N. Clauvelin, ..., M. Wardetzky. 2013. A discrete geometric approach for simulating the dynamics of thin viscous threads. *J. Comput. Phys.* 253:18–49.
47. Cao, L. G., and Y. L. Wang. 1990. Mechanism of the formation of contractile ring in dividing cultured animal cells. II. Cortical movement of microinjected actin filaments. *J. Cell Biol.* 111:1905–1911.
48. Hickson, G. R. X., A. Echard, and P. H. O'Farrell. 2006. Rho-kinase controls cell shape changes during cytokinesis. *Curr. Biol.* 16:359–370.
49. Loria, A., K. M. Longhini, and M. Glotzer. 2012. The RhoGAP domain of CYK-4 has an essential role in RhoA activation. *Curr. Biol.* 22:213–219.
50. Lekomtsev, S., K.-C. Su, ..., M. Petronczki. 2012. Centralspindlin links the mitotic spindle to the plasma membrane during cytokinesis. *Nature.* 492:276–279.
51. Argiros, H., L. Henson, ..., C. B. Shuster. 2012. Centralspindlin and chromosomal passenger complex behavior during normal and Rappaport furrow specification in echinoderm embryos. *Cytoskeleton (Hoboken).* 69:840–853.
52. Carvalho, A., A. Desai, and K. Oegema. 2009. Structural memory in the contractile ring makes the duration of cytokinesis independent of cell size. *Cell.* 137:926–937.
53. Yoneda, M., and K. Dan. 1972. Tension at the surface of the dividing sea-urchin egg. *J. Exp. Biol.* 57:575–587.
54. Reymann, A.-C., R. Boujemaa-Paterski, ..., L. Blanchoin. 2012. Actin network architecture can determine myosin motor activity. *Science.* 336:1310–1314.
55. Mishra, M., J. Kashiwazaki, ..., I. Mabuchi. 2013. In vitro contraction of cytokinetic ring depends on myosin II but not on actin dynamics. *Nat. Cell Biol.* 15:853–859.
56. Bray, D., and J. G. White. 1988. Cortical flow in animal cells. *Science.* 239:883–888.
57. Murrell, M. P., and M. L. Gardel. 2012. F-actin buckling coordinates contractility and severing in a biomimetic acto-myosin cortex. *Proc. Natl. Acad. Sci. USA.* 109:20820–20825.
58. Mayer, M., M. Depken, ..., S. W. Grill. 2010. Anisotropies in cortical tension reveal the physical basis of polarizing cortical flows. *Nature.* 467:617–621.
59. Fishkind, D. J., and Y. L. Wang. 1993. Orientation and three-dimensional organization of actin filaments in dividing cultured cells. *J. Cell Biol.* 123:837–848.
60. Moulding, D. A., E. Moeendarbary, ..., A. J. Thrasher. 2012. Excess F-actin mechanically impedes mitosis leading to cytokinesis failure in X-linked neutropenia by exceeding Aurora B kinase error correction capacity. *Blood.* 120:3803–3811.
61. Yeung, A., and E. Evans. 1989. Cortical shell-liquid core model for passive flow of liquid-like spherical cells into micropipets. *Biophys. J.* 56:139–149.
62. Daniels, B. R., B. C. Masi, and D. Wirtz. 2006. Probing single-cell micromechanics in vivo: the microrheology of *C. elegans* developing embryos. *Biophys. J.* 90:4712–4719.
63. Charras, G. T., T. J. Mitchison, and L. Mahadevan. 2009. Animal cell hydraulics. *J. Cell Sci.* 122:3233–3241.
64. Kalwarczyk, T., N. Ziebarcik, ..., R. Hołyst. 2011. Comparative analysis of viscosity of complex liquids and cytoplasm of mammalian cells at the nanoscale. *Nano Lett.* 11:2157–2163.
65. Spek, J. 1918. Surface tension differences as a cause of cell division [Oberflächenspannungsdifferenzen als eine Ursache der Zellteilung]. *Arch. Entwicklungsmech. Org.* 44:5–113.
66. Dan, K., T. Yanagita, and M. Sugiyama. 1937. Behavior of the cell surface during cleavage. I. *Protoplasma.* 28:66–81.
67. Happel, J., and H. Brenner. 1983. Low Reynolds Number Hydrodynamics. Kluwer Academic Publishers, Norwell, MA.
68. Libai, A., and J. G. Simmonds. 1995. The Nonlinear Theory of Elastic Shells. Cambridge University Press, Cambridge, UK.
69. Salbreux, G., G. Charras, and E. Paluch. 2012. Actin cortex mechanics and cellular morphogenesis. *Trends Cell Biol.* 22:536–545.
70. Clark, A. G., K. Dierkes, and E. K. Paluch. 2013. Monitoring actin cortex thickness in live cells. *Biophys. J.* 105:570–580.

SUPPORTING MATERIAL FOR: Furrow constriction in animal cell cytokinesis

Hervé Turlier,^{†*} Basile Audoly,[‡] Jacques Prost,^{†§} and Jean-François Joanny[†]

[†]Physicochimie Curie (CNRS-UMR168),
Institut Curie, Section de Recherche,
26 rue d'Ulm, 75248 Paris Cedex 05, France,

[‡]Institut Jean Le Rond d'Alembert (CNRS-UMR7190),
UPMC Université Paris 06,
4 Place Jussieu 75252 Paris Cedex 05, France,

[§]ESPCI-ParisTech,
10 Rue Vauquelin, 75231 Paris Cedex 05, France

*Correspondence: herve.turlier@polytechnique.org

This document contains:

- A Model Supplement and Supporting References
- Tables S1 and S2
- Figures S1 to S6
- Still images and legends for Movies S1 to S5

MODEL SUPPLEMENT

1 Continuous model

1.1 Model hypothesis

Negligible cytoplasmic dissipation Flows of the cytoplasm in cytokinesis are triggered by compression in the furrow region and by advection by cortical flows in polar regions. No matter which one of these processes is dominant, cytoplasmic flows are therefore passively driven by an active cortical flow of typical value v_a . The order of magnitude of the strain rate of cytoplasmic flows is therefore $\frac{v_a}{R}$, where R is the mean curvature radius of the polar regions. Note that this scaling law also gives the strain rate of cortical flows from the poles toward the equator. Cytoplasmic flows operate on volumes of the order of cell volume R^3 , whereas the typical cortical volume is $R^2 e_0$, where e_0 is the cortical thickness. We evaluate therefore the two sources of dissipation as follows

$$\mathcal{D}_{\text{cytoplasm}} \approx \eta_{\text{cytoplasm}} R^3 \left(\frac{v_a}{R} \right)^2, \quad (\text{S1a})$$

$$\mathcal{D}_{\text{cortex}} \approx \eta_{\text{actomyosin}} R^2 e_0 \left(\frac{v_a}{R} \right)^2. \quad (\text{S1b})$$

The ratio of the two sources of viscous dissipation, cytoplasmic and actomyosin cortical flows, scales finally as

$$\frac{\mathcal{D}_{\text{cytoplasm}}}{\mathcal{D}_{\text{cortex}}} \approx \frac{\eta_{\text{cytoplasm}}}{\eta_{\text{actomyosin}}} \frac{R}{e_0}. \quad (\text{S2})$$

which is identical to the formula derived by Yeung and Evans in a more detailed analysis (1). The viscosity of the cortex is of the order of $10^5\text{-}10^6 \text{ Pa.s}$ (Table S1), whereas the cytoplasmic viscosity is of the order of $10^{-2}\text{-}10^1 \text{ Pa.s}$ (2–4). In spite of a high volume ratio $R/e_0 \approx 10^2$ (see Table S1), the viscous dissipation in the cytoplasm remains therefore generally negligible compared to the dissipation in the cortex during cytokinesis: $\mathcal{D}_{\text{cytoplasm}} \ll \mathcal{D}_{\text{cortex}}$.

We see from (Eq. S2) that for very big cells, the viscous dissipation in the cytoplasm might become important. We consider as an example an extreme case, a *Xenopus Laevis* egg, which might be the largest animal egg, with a diameter $R \sim 1 \text{ mm}$. Its cortex has a thickness e of the order of $\sim 100 \text{ nm}$ (23) and a viscosity at minimum 10^5 Pa.s . In normal conditions, the cytoplasm is expected to have a viscosity of the order of 10^1 Pa.s at most. The ratio (Eq. S2) would then be of order ~ 1 , indicating that viscous dissipation in the cytoplasm should start to be taken into account. Most of the cell lines studied have generally a diameter smaller than $100 \mu\text{m}$ and the assumption of negligible cytoplasmic dissipation is not very restrictive.

Negligible friction on the plasma membrane A further possible source of dissipation is the friction of the cortex on the plasma membrane. In *C. Elegans* embryos, Mayer et al. (6) evaluated experimentally the hydrodynamic length scale of cortical flows $l \equiv \sqrt{\eta^{2D}/\gamma}$, where $\eta^{2D} \sim e_0 \eta_{\text{actomyosin}}$ is the 2D effective viscosity of the cortical layer and γ characterizes the frictional forces associated with cortical sliding along the cell membrane and the cytoplasm. The hydrodynamic length scale evaluates the typical length over which viscous dissipation dominates over frictional losses. Their measurements led to $l \approx 14 \mu\text{m}$, which is about the embryo size: it indicates that friction forces are not limiting the cortical flow and hence can be neglected compared to cortical viscous forces. More generally the extension of cortical flows over the entire cell during cytokinesis, as early reported in sea-urchin eggs (7–9), reveals negligible friction losses compared to cortical viscous dissipation.

1.2 Lagrangian formulation of an axisymmetric visco-active membrane shell

We follow the geometric approach developed originally in (10) to describe the dynamics of thin viscous threads, and we adapt it to axisymmetric thin shells. The mechanical equilibrium of viscous thin shells is

given by the balance of forces normal and tangential to the shell contour. Because the shell remains thin, stresses can be integrated over its thickness, which leads to tensions acting tangentially to the shell mid-surface (11). A membrane is a thin shell where the contribution of bending moments and transverse shear components are negligible compared to in-plane tensions (11). The cortical layer was already described by an Eulerian membrane theory by Yeung and Evans (1), and by a thin shell theory, explicitly derived by Salbreux (12) from the active-gel rheology (13), but with fixed thickness (no turnover) and at leading order in perturbation. We elaborate here continuous and discrete Lagrangian membrane formulations, allowing for shell thickness variations via explicit turnover, and we solve the problem numerically in the regime of large deformations and large displacements.

1.2.1 Lagrangian description

A Lagrangian description requires the definition of a reference state. It is chosen here to be spherical, corresponding to the metaphase cell shape, right before cytokinesis onset. Since the membrane remains axisymmetric, its shape in 3D can be reconstructed by revolving a base curve about the z -axis \mathbf{e}_z (Fig. S1 A and Movie S5). We call φ the azimuthal angle. We consider therefore only a section plane ($\mathbf{e}_z, \mathbf{e}_r(\varphi)$) perpendicular to the azimuthal direction $\mathbf{e}_\varphi(\varphi)$ (Fig. S1 A).

We call S the Lagrangian curvilinear coordinate in the reference state of the membrane, to distinguish from the Eulerian curvilinear or contour length s used in the main text and defined in the next section.

Spatial and temporal derivatives of any function $f(S, t)$ are defined by

$$f'(S, t) = \frac{\partial f(S, t)}{\partial S}, \quad (\text{S3a})$$

$$\dot{f}(S, t) = \frac{\partial f(S, t)}{\partial t}. \quad (\text{S3b})$$

Since S is a Lagrangian variable, the time derivative is a *material* derivative - often written $\dot{f}(S, t) = \frac{Df(s, t)}{Dt}$ in an Eulerian formulation - and describes the rate of change of f as one follows a particle.

1.2.2 Membrane kinematics

In actual configuration, the position of the membrane reads

$$\mathbf{x}(S, t) = z(S, t) \mathbf{e}_z + r(S, t) \mathbf{e}_r(\varphi). \quad (\text{S4})$$

Its first and second time derivatives are the *material* velocity and acceleration:

$$\mathbf{u}(S, t) = \dot{\mathbf{x}}(S, t) = (\dot{z}(S, t), \dot{r}(S, t)), \quad (\text{S5a})$$

$$\ddot{\mathbf{x}}(S, t) = \dot{\mathbf{u}}(S, t) = (\ddot{z}(S, t), \ddot{r}(S, t)). \quad (\text{S5b})$$

We define the local Frenet frame $(\mathbf{t}, \mathbf{n}, \mathbf{e}_\varphi)$, where \mathbf{t} and \mathbf{n} are the unit vectors tangent and normal to the midline (Fig. S1 A).

$$\mathbf{t}(S, t) = \frac{\mathbf{x}'}{|\mathbf{x}'|} = \frac{\mathbf{x}'(S, t)}{\ell(S, t)}, \quad (\text{S6a})$$

$$\mathbf{n}(S, t) = \mathbf{e}_\varphi \times \mathbf{t}(S, t). \quad (\text{S6b})$$

where $\ell(S, t) = |\mathbf{x}'(S, t)|$ measures the stretch of the base curve, compared to the reference configuration.

We define the curvilinear or contour length s (Main text Eq. 2 and *(inset)* of Figs. 3 A, 4 and 5) using the equator as the origin: $s(S, t) = \int_{S_{\text{eq}}}^S dS' \ell(S', t)$, where S_{eq} denotes the Lagrangian coordinate of the equator.

The area of the membrane per unit dS and $d\varphi$ is given by

$$a = |\mathbf{x}' \times \mathbf{x}_{,\varphi}| = |\ell \mathbf{t} \times (-r \mathbf{e}_\varphi)| = \ell(S, t) r(S, t). \quad (\text{S7})$$

where $f_{,\varphi} \equiv \frac{\partial f}{\partial \varphi}$

The rate of membrane stretching reads therefore

$$\frac{\dot{a}}{a} = \frac{\dot{\ell}}{\ell} + \frac{\dot{r}}{r}, \quad (\text{S8})$$

where $\dot{\ell} = \left| \frac{\partial^2 \mathbf{x}}{\partial S \partial t} \right| = \left| \frac{\partial \mathbf{u}}{\partial S} \right| = \mathbf{t} \cdot \frac{\partial \mathbf{u}}{\partial S}$.

By identification we deduce the two components $d_s + d_\varphi = \frac{\dot{a}}{a}$ of the membrane strain rate in axial direction \mathbf{t} and azimuthal direction \mathbf{e}_φ

$$d_s(S, t) = \frac{\dot{\ell}}{\ell} = \mathbf{t} \cdot \left(\frac{1}{\ell} \frac{\partial \mathbf{u}}{\partial S} \right), \quad (\text{S9a})$$

$$d_\varphi(S, t) = \frac{\dot{r}}{r} = \mathbf{e}_r \cdot \frac{\mathbf{u}}{r}. \quad (\text{S9b})$$

1.2.3 Membrane tensions

The tension in the membrane is obtained by integrating the bulk actomyosin stress $\sigma_{\alpha\beta}$ in its transverse dimension ξ along \mathbf{n} . Given that the cortex remains thin relative to the cell radius, we only keep the first order in thickness $e(S, t)$ in a membrane theory. Axial and azimuthal tension components read, respectively,

$$N_s(S, t) = \int_{-e/2}^{e/2} d\xi \sigma_{ss}(\xi) \approx e \sigma_{ss}(0), \quad N_\varphi(S, t) = \int_{-e/2}^{e/2} d\xi \sigma_{\varphi\varphi}(\xi) \approx e \sigma_{\varphi\varphi}(0). \quad (\text{S10})$$

where the mid-surface is defined at $\xi = 0$. The stress in an actomyosin gel is the sum of viscous and active components, as explained below.

2D reduction of the viscous constitutive law We write the constitutive relation for a Stokean fluid in 3 dimensions (14)

$$\sigma_{\alpha\beta}^v = 2\eta u_{\alpha\beta}^v - p \delta_{\alpha\beta}, \quad (\text{S11})$$

where $\sigma_{\alpha\beta}^v$ is the viscous contribution to the bulk viscous stress in the gel, p the bulk pressure and $u_{\alpha\beta}^v \equiv \frac{1}{2} (\partial_\alpha u_\beta + \partial_\beta u_\alpha)$ the symmetric part of the bulk strain rate tensor in the gel.

In the Frenet frame $(\mathbf{t}, \mathbf{n}, \mathbf{e}_\varphi)$, the incompressibility of the gel reads

$$u_{ss}^v + u_{\varphi\varphi}^v + u_{nn}^v = 0. \quad (\text{S12})$$

The normal component of the stress vanishes at the free boundaries $\sigma_{nn}(e/2) = \sigma_{nn}(-e/2) = 0$ and is considered uniform along the transverse direction in a membrane theory (lubrication hypothesis). We deduce the bulk pressure

$$p \approx 2\eta u_{nn}^v = -2\eta (u_{ss}^v + u_{\varphi\varphi}^v). \quad (\text{S13})$$

The membrane's strain rates in the axial and azimuthal directions are defined by averaging the bulk strain rate over the thickness, and can be identified with strain rates at the mid-surface at the dominant order, $d_s = \frac{1}{e} \int_{-e/2}^{e/2} d\xi u_{ss}(\xi) \approx u_{ss}^v(0)$ and $d_\varphi = \frac{1}{e} \int_{-e/2}^{e/2} d\xi u_{\varphi\varphi}(\xi) \approx u_{\varphi\varphi}^v(0)$. This yields the effective 2D viscosity law for the membrane,

$$N_s^v = 2\eta e (2d_s + d_\varphi), \quad (\text{S14a})$$

$$N_\varphi^v = 2\eta e (d_s + 2d_\varphi). \quad (\text{S14b})$$

Active constitutive law A nematic theory of active gels (13) predicts an active stress dominant contribution of the general form

$$\sigma_{\alpha\beta}^a = \zeta \Delta\mu Q_{\alpha\beta}, \quad (\text{S15})$$

where $Q_{\alpha\beta} \equiv \langle p_\alpha p_\beta - \frac{1}{3}\delta_{\alpha\beta} \rangle$ is the nematic order parameter, $\zeta > 0$ is a measure of the local motor contractile activity, $\Delta\mu$ is the chemical free energy for one ATP molecule hydrolysis and p_α is a vector representing the local polarity of filaments. We make the simplifying assumption that actin filaments remain parallel to the membrane mid-plane and that their polarization remains isotropic within the membrane plane. This implies $Q_{ss} = Q_{\varphi\varphi} = \frac{1}{2}$ and $Q_{nn} = 0$.

The active contribution to the membrane tension is therefore isotropic and reads

$$N_s^a = N_\varphi^a \approx e \sigma_{ss}^a(0) = e \sigma_{\varphi\varphi}^a(0) = \frac{e}{2} \zeta(S, t) \Delta\mu. \quad (\text{S16})$$

Membrane total tension The total tensions in the membrane are the sum of the active (Eq. S16) and viscous (Eq. S14) contributions and read (Main text Eq. 2)

$$N_s = \frac{e}{2} \zeta \Delta\mu + 2\eta e (2d_s + d_\varphi), \quad (\text{S17a})$$

$$N_\varphi = \frac{e}{2} \zeta \Delta\mu + 2\eta e (d_s + 2d_\varphi). \quad (\text{S17b})$$

1.2.4 Turnover dynamics

The cortical actomyosin is under permanent turnover. The source term, due to actin polymerization, is proportional to the membrane surface since polymerization nucleators are located near the plasma membrane. We describe this effect via a polymerization velocity v_p from the shell upper surface $\xi = e/2$. By contrast depolymerization acts in volume and leads to a depolymerization rate k_d . The transverse strain rate in the membrane is therefore the sum of a viscous contribution and turnover term, whereas other strain rate components remain identical

$$u_{nn} = u_{nn}^v + \left[v_p \delta \left(\xi - \frac{e}{2} \right) - k_d \right], \quad (\text{S18})$$

where $\delta(x)$ is a Delta function of x .

We average over the membrane thickness the equation of incompressibility projected on the local Frenet frame $(\mathbf{t}, \mathbf{n}, \mathbf{e}_\varphi)$, which leads to

$$u_{ss}(0) + u_{nn}(0) + u_{\varphi\varphi}(0) = \frac{v_p}{e} - k_d. \quad (\text{S19})$$

We consider a element of membrane of volume $a e = \ell(S, t) r(S, t) e(S, t)$ per unit dS and $d\varphi$, where the element of surface a is defined in Eq. S7. We identify the rate of surface stretching $d_s + d_\varphi = u_{ss}^v(0) + u_{\varphi\varphi}^v(0) = u_{ss}(0) + u_{\varphi\varphi}(0) = \frac{\dot{a}}{a}$ and the rate of thickness variation $u_{nn}(0) = \frac{\dot{e}}{e}$. We deduce the Lagrangian rate of variation of the element of membrane volume ae under both effects of incompressibility and turnover (Main text Eq. 3)

$$\frac{d(ae)}{dt} = -k_d ae + v_p a. \quad (\text{S20})$$

1.3 Balance of forces

We use the principle of virtual work for thin membranes, as it provides a natural way to obtain the equations of motion for discrete membranes. For any virtual motion of the membrane $\hat{\mathbf{u}}(S, t) = \hat{\mathbf{x}}$ subject to the constraint of incompressibility, the balance of forces in weak form reads (Einstein notation) (15)

$$-\oint dA N_{\alpha\beta} \hat{d}_{\alpha\beta} - K(\mathcal{V} - \mathcal{V}_0) \hat{\mathcal{V}} = 0. \quad (\text{S21})$$

where $\hat{d}_{\alpha\beta} = \hat{u}_{\alpha\beta} = \frac{1}{2}(\partial_\alpha \hat{u}_\beta + \partial_\beta \hat{u}_\alpha)$ is the virtual strain rate, $\hat{\mathcal{V}} = \oint dA n_\beta \hat{u}_\beta$ is the virtual change of volume, and \oint is the integral on the closed membrane surface.

The divergence operator $\mathbf{div}(N_s, N_\varphi)$ is defined by the identity

$$\oint dA \mathbf{div}(N_s, N_\varphi) \cdot \hat{\mathbf{u}} = - \oint dA \left(N_s \hat{d}_s + N_\varphi \hat{d}_\varphi \right)$$

which must hold for any virtual displacement $\hat{\mathbf{u}}$ associated with the virtual strain rates \hat{d}_s and \hat{d}_φ . Inserting the explicit expressions of the virtual strain rates, we find

$$\begin{aligned} \int 2\pi r\ell dS \mathbf{div}(N_s, N_\varphi) \cdot \left(\hat{z}\mathbf{e}_z + \hat{r}\mathbf{e}_r \right) &= - \int 2\pi r\ell dS \left(N_s \frac{\mathbf{t}}{\ell} \cdot \frac{\partial \hat{\mathbf{u}}}{\partial S} + N_\varphi \frac{\hat{r}}{r} \right) \\ &= \int 2\pi r\ell dS \left\{ \hat{z} \left[-\frac{1}{r\ell} \frac{\partial}{\partial S} (rt_z N_s) \right] + \hat{r} \left[\frac{N_\varphi}{r} - \frac{1}{r\ell} \frac{\partial}{\partial S} (rt_r N_s) \right] \right\}, \end{aligned}$$

Identifying both sides, we find an explicit expression of the divergence operator (Main text Eq. 5):

$$\mathbf{div}(N_s, N_\varphi) = -\frac{1}{r\ell} \frac{\partial}{\partial S} (rt_z N_s) \mathbf{e}_z + \left(\frac{N_\varphi}{r} - \frac{1}{r\ell} \frac{\partial}{\partial S} (rt_r N_s) \right) \cdot \mathbf{e}_r. \quad (\text{S22})$$

The principle of virtual work (Eq. S21) yields the force balance for membranes. It classically reads as in (Main text Eq. 5), where the divergence operator is given here by Eq. S22 in our representation.

2 Discrete formulation

We extend here the discretization approach proposed for viscous threads (10) to the case of axisymmetric membranes, based on the previous continuous equations.

2.1 Geometrical relations

The axisymmetric membrane shell is represented by a collection of $n+1$ vertices $\{\mathbf{x}_i(t) = (r_i(t), z_i(t))\}_{0 \leq i \leq n}$ living in the half-plane $r \geq 0$ as represented on Fig. S1 B. Neighboring vertices are connected by segments. The vertices at poles \mathbf{x}_0 and \mathbf{x}_n are subjected to the constraint $r_0 = r_n = 0$.

The volume enclosed by the membrane reads

$$\mathcal{V} = \sum V^i = \sum V(\mathbf{x}_i, \mathbf{x}_{i+1}), \quad (\text{S23})$$

where the contribution associated with a segment is the volume enclosed by a truncated cone obtained by revolving the segment about the z-axis,

$$V(\mathbf{x}_i, \mathbf{x}_{i+1}) = \frac{\pi}{3} (r_i^2 + r_i r_{i+1} + r_{i+1}^2) (z_{i+1} - z_i). \quad (\text{S24})$$

Let us call \mathbf{g}_i the gradient of the enclosed volume with respect to vertex positions. It will be used to define a discrete pressure force:

$$\mathbf{g}_i = \nabla_{\mathbf{x}_i} \mathcal{V}. \quad (\text{S25})$$

It can be computed by summing contributions of the form

$$\mathbf{V}_{,i+1}(\mathbf{x}_i, \mathbf{x}_{i+1}) = \frac{\pi}{3} \left((r_i + 2r_{i+1})(z_{i+1} - z_i) \mathbf{e}_r + (r_i^2 + r_i r_{i+1} + r_{i+1}^2) \mathbf{e}_z \right), \quad (\text{S26})$$

and the symmetric formula for $V_{,i}(\mathbf{x}_i, \mathbf{x}_{i+1})$. Here, the comma in index denotes a gradient with respect to a vertex \mathbf{x}_i : $\nabla_{\mathbf{x}_i} f = f_{,\mathbf{x}_i}$.

The area of the membrane reads

$$\mathcal{A} = \sum A^i = \sum A(\mathbf{x}_i, \mathbf{x}_{i+1}), \quad (\text{S27})$$

where the contribution associated with a segment is the lateral area of a truncated cone,

$$A(\mathbf{x}_i, \mathbf{x}_{i+1}) = 2\pi \frac{r_i + r_{i+1}}{2} \ell^i, \quad (\text{S28})$$

with

$$\ell^i = \sqrt{(r_{i+1} - r_i)^2 + (z_{i+1} - z_i)^2}, \quad (\text{S29})$$

denotes the segment length.

2.2 Membrane strain rates

From the continuous formula in Eq. S9, we deduce the discrete strain rates in the axial and azimuthal directions

$$d_s^i = \frac{\dot{\ell}^i}{\ell^i} = \frac{\mathbf{t}^i \cdot (\mathbf{u}_{i+1} - \mathbf{u}_i)}{\ell^i}. \quad (\text{S30a})$$

$$d_\varphi^i = \frac{\dot{r}_i + \dot{r}_{i+1}}{r_i + r_{i+1}} = \frac{\mathbf{e}_r \cdot (\mathbf{u}_i + \mathbf{u}_{i+1})}{r_i + r_{i+1}}. \quad (\text{S30b})$$

2.3 Membrane tension

Viscous contribution From the continuous formulation in Eq. S14, the viscous contributions to the membrane tension read

$$N_s^{v,j} = 2\eta e^j (2d_s^j + d_\varphi^j), \quad N_{v\varphi}^j = 2\eta e^j (d_s^j + 2d_\varphi^j). \quad (\text{S31})$$

Active contribution From the continuous formulation in Eq. S16, the active contributions to the membrane tension read

$$N_s^{a,j} = N_\varphi^{a,j} = \frac{1}{2} e^j \zeta^j \Delta\mu. \quad (\text{S32})$$

2.4 Cytoplasmic pressure

From the continuous constitutive relation (Eq. 4 in the main text), we can express the uniform cytoplasmic pressure by summing discrete enclosed volume contributions in Eq. S24

$$P = -K \left(\sum V(\mathbf{x}_i, \mathbf{x}_{i+1}) - \mathcal{V}_0 \right). \quad (\text{S33})$$

2.5 Balance of forces

The membrane stress is described by a tensor living on segments

$$\mathbf{N}^j = N_s^j \mathbf{t}^j \otimes \mathbf{t}^j + N_\varphi^j \mathbf{e}_\varphi \otimes \mathbf{e}_\varphi, \quad (\text{S34})$$

where \mathbf{t}^j is the unit tangent vector associated to the segment j .

The principle of virtual work (Eq. S21) provides a natural way for discretizing the equations of motion: for any virtual motion of the vertices $(\hat{\mathbf{x}}_i)_{0 \leq i \leq n+1}$,

$$\sum_{\text{vert } i} P \mathbf{g}_i \cdot \hat{\mathbf{x}}_i - \sum_{\text{seg } j} \left(N_s^j \hat{d}_s^j + N_\varphi^j \hat{d}_\varphi^j \right) A^j = 0, \quad (\text{S35})$$

where P is the cytoplasmic pressure defined in Eq. S33, the virtual work of which is derived from the continuous formulation (Eq. S21): $P \hat{\mathcal{V}} = P \nabla_{\mathbf{x}_i} \mathcal{V} \cdot \hat{\mathbf{x}}_i = P \mathbf{g}_i \cdot \hat{\mathbf{x}}_i$. The virtual strain rates read, in analogy with equation (S30),

$$\hat{d}_s^j = \frac{\mathbf{t}^j \cdot (\hat{\mathbf{x}}_{j+1} - \hat{\mathbf{x}}_j)}{\ell^j} \quad (\text{S36a})$$

$$\hat{d}_\varphi^j = \frac{\mathbf{e}_r \cdot (\hat{\mathbf{x}}_j + \hat{\mathbf{x}}_{j+1})}{r_j + r_{j+1}} \quad (\text{S36b})$$

When the virtual velocities are eliminated, Eq. S35 yields a set of $2n$ equations for the $2n$ degrees of freedom of the system. These equations depend on the velocities through the constitutive laws.

2.6 Membrane incompressibility with turnover dynamics

Each segment carries a volume $w^j(t)$, which evolves in analogy with the continuous formulation (Eq. S20):

$$\dot{w}^j = -k_d w^j + v_p A^j, \quad (\text{S37})$$

where A^j is the lateral areal defined in Eq. S28.

This volume is used to reconstruct the thickness of a segment, based on the position of its end vertices:

$$e^j = \frac{w^j}{A^j}. \quad (\text{S38})$$

3 Numerical implementation

3.1 Numerical code

We adapted to axisymmetric membranes a preexisting C++ code called *DVR* (Discrete Viscous Rods), originally developed for simulating the dynamics of viscous threads (10). We implemented the discrete axisymmetric geometrical relations Eq. S23 to Eq. S31, active (Eq. S32) and cytoplasmic (Eq. S33) forces, and segment volume update (Eq. S37).

3.2 Remeshing: adaptive refinement and coarsening

Gradients of active tension trigger membrane flows and rapid accumulation of Lagrangian points toward the equatorial region, where the contractile activity is maximum, and to the depletion from regions of lowest activity. Refinement is also needed due to the large curvature in the equatorial furrow. We implemented both mesh adaptation and coarsening as follows.

Adaptive mesh refinement The procedure used for axisymmetric membranes is very similar to the original mesh refinement algorithm implemented in the *DVR* code (10). Segments that need refinement are first identified at the end of a viscous time-step. The criterion is based on the comparison of the length of the segment to some prescribed maximal length, which has been chosen as $1.5 \ell_0$ where $\ell_0 = 2\pi R_0/n_0$ is the initial length of segments (n_0 is the initial number of segments). This refinement criterion has been adjusted manually to offer the best compromise between accuracy and efficiency. A new vertex is inserted in between the two vertices of each segment that have been marked, and two new segments are allocated to replace the former one. The new vertex is inserted, two new segments are allocated and the former segment is removed. The new vertex position and velocity are calculated by an interpolation of order 2 of position and velocity of its neighboring vertices. The stretching forces which depend on the derivatives of the positions and velocities to an order up to two, remain hence smooth upon subdivision. The volume of the two new segments is finally interpolated to globally conserve volume and to result in the same membrane thickness.

Adaptive mesh coarsening The mesh coarsening procedure has been developed specifically for the present application. It follows the same lines as the previous conventional mesh refinement algorithm. At the end of a viscous time-step, the smallest segment is sought. Coarsening is applied to it when its length is below a prescribed threshold, or when the angle between its neighboring segments exceeds a threshold. This criterion triggers coarsening in the presence of large stretch, or when the curvature is large. Coarsening is applied by removing this segment and its two adjacent vertices, and replacing them by a single vertex. The position and velocity of this new vertex is interpolated again up to order 2, and the volume of the two adjacent segments are updated to conserve volume globally.

3.3 Validation: spherical contraction under uniform active tension

Analytical solution We consider a spherical isotropic active membrane enclosing a compressible fluid. Its initial radius is R_0 and the membrane shell has an initial thickness e_0 . At time $t = 0$ we apply an isotropic active tension N_0^a , and consider the spherical contraction, prescribed in spherical coordinates as

$$R(\theta_0, \varphi_0, t) = R(t) \quad (\text{S39})$$

$$\theta(\theta_0, \varphi_0, t) = \theta_0 \quad (\text{S40})$$

$$\varphi(\theta_0, \varphi_0, t) = \varphi_0 \quad (\text{S41})$$

Membrane volume dynamics with turnover (Eq. S20) reads

$$2\frac{\dot{R}}{R} + \frac{\dot{e}}{e} = -k_d + \frac{v_p}{e} \quad (\text{S42})$$

The strain rate tensor is locally isotropic,

$$\mathbf{d} = \frac{\dot{R}(t)}{R(t)} (\mathbf{e}_s \otimes \mathbf{e}_s + \mathbf{e}_\varphi \otimes \mathbf{e}_\varphi). \quad (\text{S43})$$

and so is the membrane tension tensor,

$$\mathbf{N} = (N^v + N^a) (\mathbf{e}_s \otimes \mathbf{e}_s + \mathbf{e}_\varphi \otimes \mathbf{e}_\varphi). \quad (\text{S44})$$

The viscous part is given by the constitutive law in Eq. S14 as

$$N^v = 6\eta e(t) \frac{\dot{R}(t)}{R(t)} \quad (\text{S45})$$

and the active part is prescribed as a function $N^a(t)$.

The constitutive law for the inner compressible fluid reads

$$P = -K \left(\frac{4\pi}{3} R^3(t) - V_0 \right) \quad (\text{S46})$$

From the weak formulation of equilibrium (Eq. S21), balance of forces reads

$$P = \frac{2}{R(t)} N_0^a \quad (\text{S47})$$

Combining the previous equations we get a system of two coupled ordinary differential equations (o.d.e.) governing the time evolution of the radius and the thickness

$$N_v + N_0^a = 6\eta e(t) \frac{\dot{R}(t)}{R(t)} + N_0^a = -K \frac{R(t)}{2} \left(\frac{4\pi}{3} R^3(t) - V_0 \right) \quad (\text{S48a})$$

$$2\frac{\dot{R}(t)}{R(t)} + \frac{\dot{e}(t)}{e(t)} = -k_d + \frac{v_p}{e(t)} \quad (\text{S48b})$$

Validation procedure We validate our implementation of the compressible cytoplasm and of turnover by comparing a numerical solution to the ordinary differential equations in Eq. S48 obtained using Mathematica® 9.0.1., to the results of the simulation. We plot a comparison of numerical and analytical results for various values of K at fixed turnover in Fig. S6 A and for various $k_d > 0$ and $v_p > 0$ at fixed K in Fig. S6 B (see Figures).

3.4 Stability

A dimension analysis of the problem leads to three typical time-scales:

- An active time-scale

$$T_a = \frac{e_0 \eta}{N_0^a} = \frac{2\eta}{\zeta_0 \Delta \mu}, \quad (\text{S49})$$

that characterizes the typical time for viscous deformation of the actomyosin gel submitted to a basal active stress $\zeta_0 \Delta \mu / 2$. For any activity ζ , one can define a corresponding active time scale $T_a(\zeta) = 2\eta/\zeta \Delta \mu$. T_a is therefore the longest active time-scale in our problem, since from Eq. 2 of the main text $\zeta(S, t) \geq \zeta_0$.

- A cytoplasmic compressibility time-scale

$$T_K = \frac{\eta e_0}{R_0 V_0 K}, \quad (\text{S50})$$

that compares the cortex deformation time scale to the cytoplasmic pressure response.

- A turnover time-scale

$$\frac{1}{k_d}, \quad (\text{S51})$$

that characterizes the typical time for the layer thickness relaxation.

Active layer intrinsic instability

We first compare the turnover and active time-scales. An active viscous layer with variable thickness is intrinsically unstable without turnover: any spatial difference in thickness creates a tension gradient that triggers an active flow toward the regions of higher thickness. The thickness increase enhances the gradient of tension and therefore amplifies itself via the cortical flow. Turnover stabilizes this effect if thicker regions depolymerize rapidly enough and thinner regions regrow rapidly enough. The active layer remains therefore stable if $T_a k_d \gg 1$.

Compressibility time-scale

We compare the compressibility time-scale T_K to the active time-scale T_a . The ratio $\frac{T_K}{T_a} = \frac{e_0}{R_0} \frac{\zeta_0 \Delta \mu}{V_0 K}$ compares active tension of the layer and cytoplasmic pressure. To avoid collapse of the membrane it has therefore to be lower than one.

Code general stability

The time-step has to be smaller than all other time-scales in the problem. Taking into account the previous stability requirements we end up with the following global requirement for code stability

$$dt \ll T_K < \frac{1}{k_d} \ll T_a. \quad (\text{S52})$$

3.5 Choice of numerical parameters

The values of numerical parameters are chosen relatively to a scale of reference. We naturally choose the initial cell radius R_0 as length-scale of reference, and the active time at poles $T_a = \frac{2\eta}{\zeta_0 \Delta \mu}$ as the time-scale of reference. We pick realistic estimates of the relative numerical parameters from various references as summarized in Table S1. We summarize in Table S2 all the sets of numerical parameters used for generating the figures and movies in this paper.

4 Scaling model

We detail here the calculations of the scaling model on the minimal geometry sketched in Fig. 6 *A* (Main Text).

4.1 Static analysis

Cytoplasmic volume conservation imposes a relation between the pole radius R and the initial cell size R_0 of the form

$$R_0^3 = R^3 \left[1 + \frac{3}{2} \cos \theta - \frac{1}{2} \cos^3 \theta \right] \equiv R^3 F(\theta) \quad (\text{S53})$$

In Fig. 6 *B*, the disappearance of the local minimum $\theta > 0$ in the energy $\mathcal{E}/\mathcal{E}_0$ when κ is increased above some threshold defines a critical point (κ_c, θ_c) . This critical point, where the final cell jumps from an incomplete constriction to a full division, is given by

$$0 = \frac{\partial \mathcal{E}}{\partial \theta} \Big|_{\theta_c}, \quad 0 = \frac{\partial^2 \mathcal{E}}{\partial \theta^2} \Big|_{\theta_c}. \quad (\text{S54})$$

Using Mathematica® 9.0.1 we solve this system of equations and get the following numerical values for complete constriction threshold $\kappa_c \approx 0.4053$, corresponding to a constriction state $\theta_c \approx 46.46^\circ$ or equivalently $r_{f_c} = 0.5884 R_0$.

4.2 Dynamics

We evaluate the power dissipated by viscous effects as defined in Eq. 9 in the main text. After calculation it reads

$$\mathcal{P}_d = 4\pi e_0 \eta \left(\frac{dr_f}{dt} \right)^2 \left[(1 + \cos \theta) + \lambda \frac{F(\theta)^{1/3}}{\sin \theta} \right], \quad (\text{S55})$$

where we defined the parameter

$$\lambda \equiv \frac{w}{2R_0} \frac{e_f}{e_0}. \quad (\text{S56})$$

We calculate the time variation of the mechanical energy $\frac{d\mathcal{E}}{dt} = -\mathcal{P}_d$ rescaled by \mathcal{E}_0 :

$$\begin{aligned} \frac{1}{\mathcal{E}_0} \frac{d\mathcal{E}}{dt} &= \frac{\partial \mathcal{E}/\mathcal{E}_0}{\partial \theta} \frac{\partial \theta}{\partial r_f} \frac{dr_f}{dt} \\ &= -\frac{\mathcal{P}_d}{\mathcal{E}_0} \\ &= -\frac{T_a}{R_0^2} \left(\frac{dr_f}{dt} \right)^2 \left[(1 + \cos \theta) + \lambda \frac{F(\theta)^{1/3}}{\sin \theta} \right], \end{aligned}$$

with $T_a = \frac{\eta e_0}{N_0^a}$ as in the continuous formulation. It leads to

$$\begin{aligned} \frac{T_a}{R_0} \frac{dr_f}{dt} &= -\frac{\partial \mathcal{E}/\mathcal{E}_0}{\partial \theta} \left(\frac{\partial r_f/R_0}{\partial \theta} \right)^{-1} \left[(1 + \cos \theta) + \lambda \frac{F(\theta)^{1/3}}{\sin \theta} \right]^{-1} \\ &\equiv -\mathcal{H}(\theta, \kappa, \lambda). \end{aligned} \quad (\text{S57})$$

Since $\mathcal{E}/\mathcal{E}_0$ depends only on θ and κ according to equation (9) in the main text, the rate of constriction reduces to a simple function \mathcal{H} of θ , κ and λ only. One can solve for the radius of the contractile ring as a function of time for given values of κ and λ by inserting $r_f/R_0 = \sin \theta F(\theta)^{-1/3}$ in Eq. S57, integrating numerically the non-linear differential equation for $\theta(t)$ and recalculating $r_f(\theta(t))$.

One should note that κ and λ are not independent in the continuous model. In particular $\lambda \propto \frac{e_f}{e_0}$ should increase with $\kappa \propto N_f^a - N_0^a$ at fixed turnover because of increased cortical flows that we neglected here. Conversely, κ depends on the ratio e_f/e_0 as we show using the continuous expressions for active tensions:

$$\begin{aligned}\kappa &\approx \frac{w}{2R_0} \frac{N_f^a - N_0^a}{N_0^a}, \\ &\approx \frac{w}{2R_0} \left(\frac{\zeta_f e_f}{\zeta_0 e_0} - 1 \right),\end{aligned}\tag{S58}$$

where ζ_f and ζ_0 are the activities respectively in the furrow and at poles.

We solve numerically Eq. S57 with Mathematica® 9.0.1., varying the activity in the furrow ζ_f/ζ_0 or its width w/R_0 to mimick the RhoA-GTP signal and the furrow thickness e_f/e_0 to mimick the effect of turnover. Results are plotted in Fig. 7 (Main text).

SUPPORTING REFERENCES

1. Yeung, A., and E. Evans. 1989. Cortical shell-liquid core model for passive flow of liquid-like spherical cells into micropipets. *Biophys. J.*, 56(1):139–49.
2. Daniels, B.R., B.C. Masi, and D. Wirtz. 2006. Probing single-cell micromechanics in vivo: the microrheology of *C. elegans* developing embryos. *Biophys. J.* 90(12):4712–4719.
3. Charras, G.T., T.J. Mitchison, and L. Mahadevan. 2009. Animal cell hydraulics. *J. Cell Sci.* 122(18):3233–3241.
4. Kalwarczyk, T., N. Zie, R. Hozyst, and C.S. Wyszy. 2011. Comparative Analysis of Viscosity of Complex Liquids and Cytoplasm. *Nano Lett.* 11(5):2157–2163.
5. Zhang, W., and D.N. Robinson. 2005. Balance of actively generated contractile and resistive forces controls cytokinesis dynamics *Proc. Natl. Acad. Sci. USA* 102(20):7186–7191.
6. Mayer, M., M. Depken, J.S. Bois, F. Julicher, and S.W. Grill. 2010. Anisotropies in cortical tension reveal the physical basis of polarizing cortical flows. *Nature* 467(7315):617–21.
7. Spek, J. 1918. Oberflchenspannungsdifferenzen als eine Ursache der Zellteilung. *Archiv fr Entwicklungsmechanik der Organismen* 44(1):5–113.
8. Dan, K., T. Yanagita, and M. Sugiyama. 1937. Behavior of the cell surface during cleavage. I. *Protoplasma* 28(1):66–81.
9. Hiramoto, Y. 1958. A quantitative description of protoplasmic sea-urchin egg. *The Journal of Experimental Biology* 35(2):407–424.
10. Audoly, B., N. Clauvelin, P-T. Brun, M. Bergou, E. Grinspun, and M. Wardetzky. 2013. A discrete geometric approach for simulating the dynamics of thin viscous threads. *J. Comput. Phys.* 253:18–49 (in press doi:10.1016/j.jcp.2013.06.034).
11. Green, A.E., and W. Zerna. 2002. *Theoretical Elasticity*, Dover Publications, pp. 386–389. New-York, 386-389.
12. Salbreux, G., J. Prost, J-F. Joanny. 2009. Hydrodynamics of Cellular Cortical Flows and the Formation of Contractile Rings. *Phys. Rev. Lett.* 103(5):058102.
13. Kruse, K., J-F. Joanny, F. Julicher, J. Prost, and K. Sekimoto. 2005. Generic theory of active polar gels : a paradigm for cytoskeletal dynamics. *Eur. Phys. J. E Soft Matter* 16(1):5–16.
14. Happel, J., and H. Brenner. 1983. *Low Reynolds Number Hydrodynamics*, Kluwer Academic Publishers, Norwell.
15. Libai, A., and J.G. Simmonds. 1995. *The Nonlinear Theory of Elastic Shells*, Cambridge University Press, Cambridge.
16. Bement, W.M., H. Benink, and G. von Dassow. 2005. A microtubule-dependent zone of active RhoA during cleavage plane specification. *J. Cell Biol.* 170(1):91–101.
17. Von Dassow, G., K.J.C Verbrugghe, A.L. Miller, J.R. Sider, and W.M. Bement. 2009. Action at a distance during cytokinesis. *J. Cell Biol.* 187(6):831–845.
18. Tinevez, J.Y., U. Schulze, G. Salbreux, J. Roensch, J-F. Joanny, and E. Paluch. 2009. Role of cortical tension in bleb growth. *Proc. Natl. Acad. Sci. USA* 106(44):18581–18586.
19. Guha, M., M. Zhou, and Y. Wang. 2005. Cortical Actin Turnover During Cytokinesis Requires Myosin II. *Curr. Biol.* 15(8):732–736.

20. Murthy, K., and P. Wadsworth. 2005. Myosin-II-dependent Localization and Dynamics of F-actin During Cytokinesis. *Curr. Biol.* 15(8):724–731.
21. Fritzsche, M., A. Lewalle, T. Duke, K. Kruse, and G. Charras. 2013. Analysis of Turnover Dynamics of the Submembranous Actin Cortex. *Mol. Biol. Cell* 24:757–767.
22. Salbreux, G., G. Charras, and E. Paluch. 2012. Actin Cortex Mechanics and Cellular Morphogenesis. *Trends Cell Biol.* 22(10):536–545.
23. Clark, A.G., K. Dierkes, and E.K. Paluch. 2013. Monitoring Actin Cortex Thickness in Live Cells. *Biophys. J.* 105(3):570–580.
24. Argiros, H., L. Henson, C. Holguin, V. Foe, and C.B. Shuster. 2012. Centralspindlin and chromosomal passenger complex behavior during normal and Rappaport furrow specification in echinoderm embryos. *Cytoskeleton (Hoboken)* 69(10):840-853.

SUPPORTING TABLES

Notation	Quantity	Experimental value(s)	Numerical value(s)	Ref(s.)
R_0	Animal cell radius	$10 - 100 \mu\text{m}$	1	(16, 17)
e_0	Cortical thickness	$0.2 - 2 \mu\text{m}$	0.02	(22, 23)
w	RhoA-GTP equatorial signal width	$1 - 10 \mu\text{m}$	0.1	(16, 17)
$1/2 \zeta_0 \Delta \mu$	Basal cortical active stress	10^3 Pa	1	(18)
T_a	Typical cytokinesis time-scale	10^3 s	10	(16, 17)
$\eta = 1/2 \zeta_0 \Delta \mu T_a$	Actomyosin viscosity	10^6 Pa s	10	/
$k_d = \log 2 / \tau_{\text{FRAP}}^{1/2}$	Depolymerization rate	0.04 s^{-1}	4	(19–21)
$v_p = e_0 k_d$	Polymerization velocity	$0.008 - 0.08 \mu\text{m s}^{-1}$	0.08	/

TABLE S1: Notations used in the main and supporting texts and their typical experimental and numerical value(s) with reference(s). Numerical values have been chosen so that $R_0 = 1$ and $T_a = 10$ are the length and time-scales of reference.

Figure(s) and movie(s)	Radius R_0	Signal amplitude $\delta\zeta^\infty$	Signal width w/R_0	Depol. rate $k_d T_a$	Bulk mod. K
Figs. 1, 2 Figs. S2, S3, S4, S5 Movies S1, S3, S5 and S2(Right)	1	75	0.1	40	250
Figs. 3 A, 3 B(<i>Inset</i>) MovieS2 (<i>Left</i>)	1	①: 10 ②: 25 ③: 40 ④: 50 ⑤: 75 ⑥: 100 MovieS2(<i>L</i>): 25	0.1	40	250
Fig. 3 B (<i>diagram</i>)	1	0 to 81 by 1	0.1	40	250
Fig. 4 MovieS4	1	75	0.1	①: 30 ②: 40 ③: 80	250
Fig. 5	(a): 0.5 (b): 1 (c): 2 (d): 4	75	(a): 0.1 (b): 0.2 (c): 0.3 (d): 0.4	40	250

TABLE S2: Numerical parameters used for generating the main text and supporting figures and movies (except for code validation, see Figs. S7A and B). The absolute or relative value of following parameters remain unchanged: $e_0/R_0 = 0.02$, $v_p = e_0 k_d$, $n_0 = 501$.

SUPPORTING FIGURES

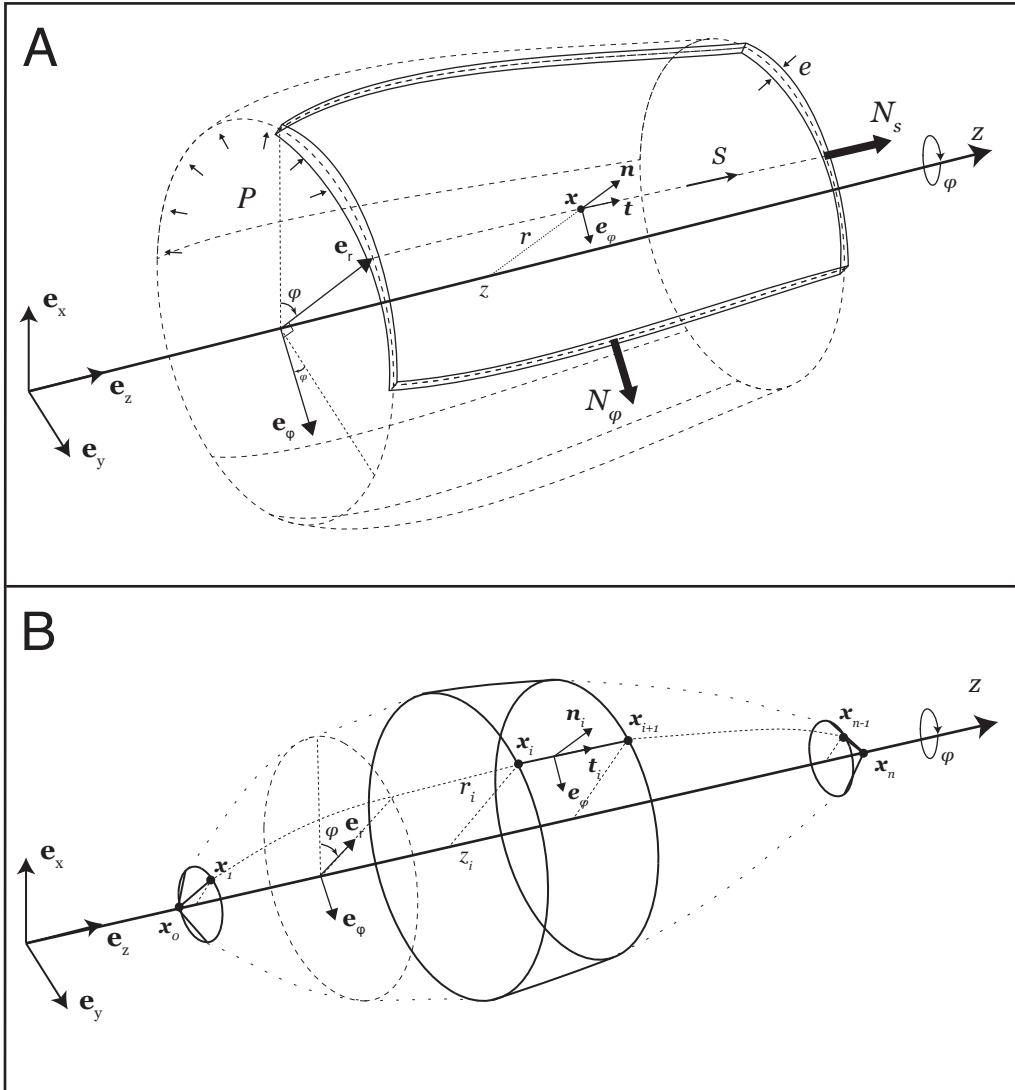


FIGURE S1: Sketch of the continuous and discrete axisymmetric membrane shell: (A) Piece of the membrane layer of thickness e . The membrane midline is parametrized by $(r(S), z(S))$ in the plane $(\mathbf{e}_z, \mathbf{e}_r)$. In the local Frenet frame $\{\mathbf{t}(S), \mathbf{n}(S), \mathbf{e}_\varphi\}$, the membrane is submitted to a tension N_s in its axial direction \mathbf{t} , to a tension N_φ in its azimuthal direction \mathbf{e}_φ and to a uniform pressure P in its normal direction \mathbf{n} . (B) Discrete axisymmetric membrane midsurface reconstructed by revolving the discrete midline $\{\mathbf{x}_i = (z_i, r_i)\}_{0 \leq i \leq n+1}$ defined in the plane $(\mathbf{e}_z, \mathbf{e}_r)$.

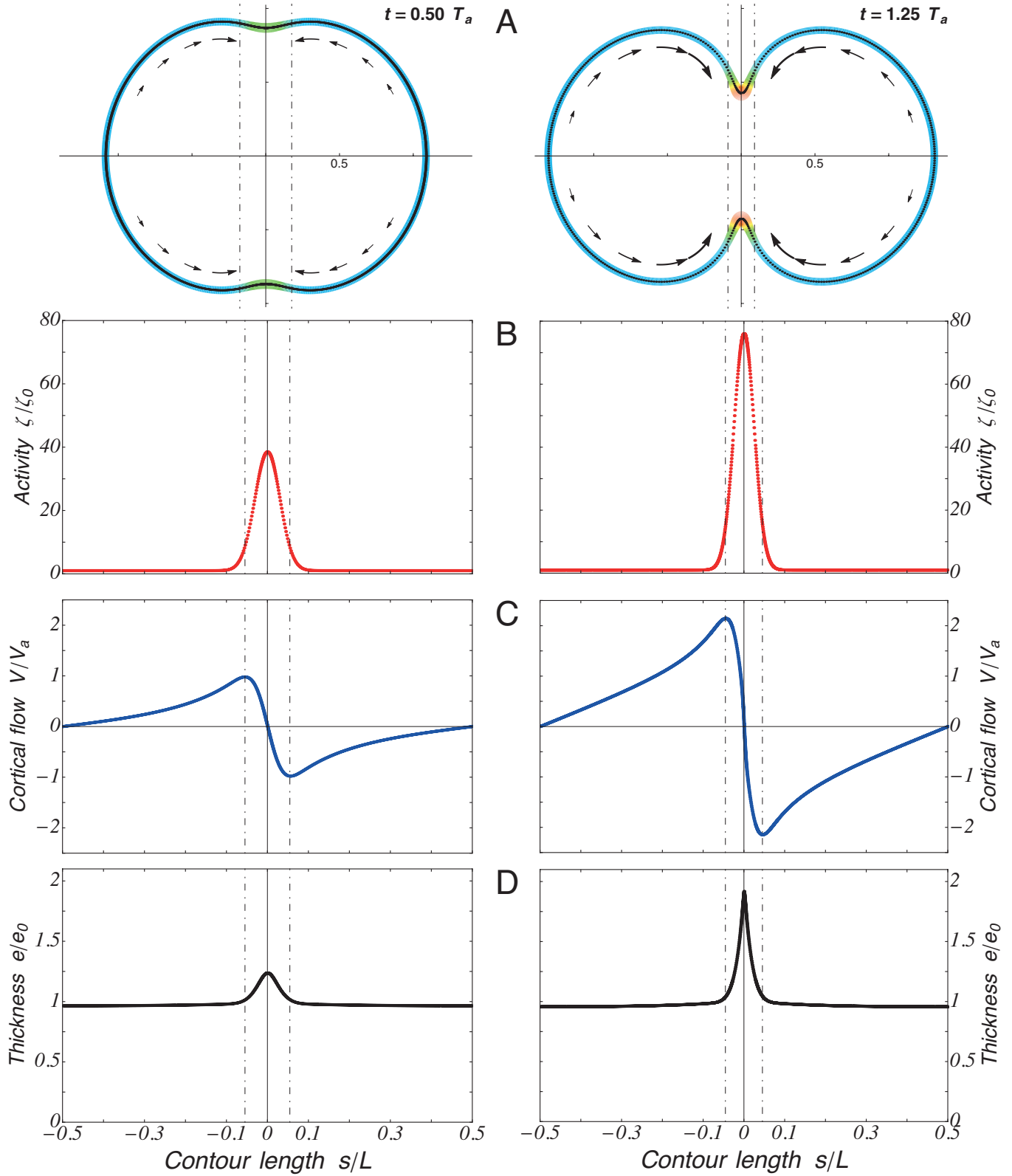


FIGURE S2: Cortical flow, furrow region and thickness: (A) Cell cortex shape and thickness at times $t = 0.5 T_a$ (left) and $t = 1.25 T_a$ (right). (B, C and D) Corresponding plots of, respectively, activity signal ζ/ζ_0 , cortical flow velocity V/V_a ($V_a = R_0/T_a$) and thickness e/e_0 along the midline contour length s/L . The cortical flow is oriented toward the furrow region and its amplitude increases with the equatorial signal between $t = 0.5 T_a$ (left) and $t = 1.25 T_a$ (right). Its extrema delimit the furrow region, demarcated by the two dot-dashed vertical lines in each figure. The increase of the cortical flow triggers a greater accumulation of actomyosin in the furrow region, leading to an expansion of its thickness.

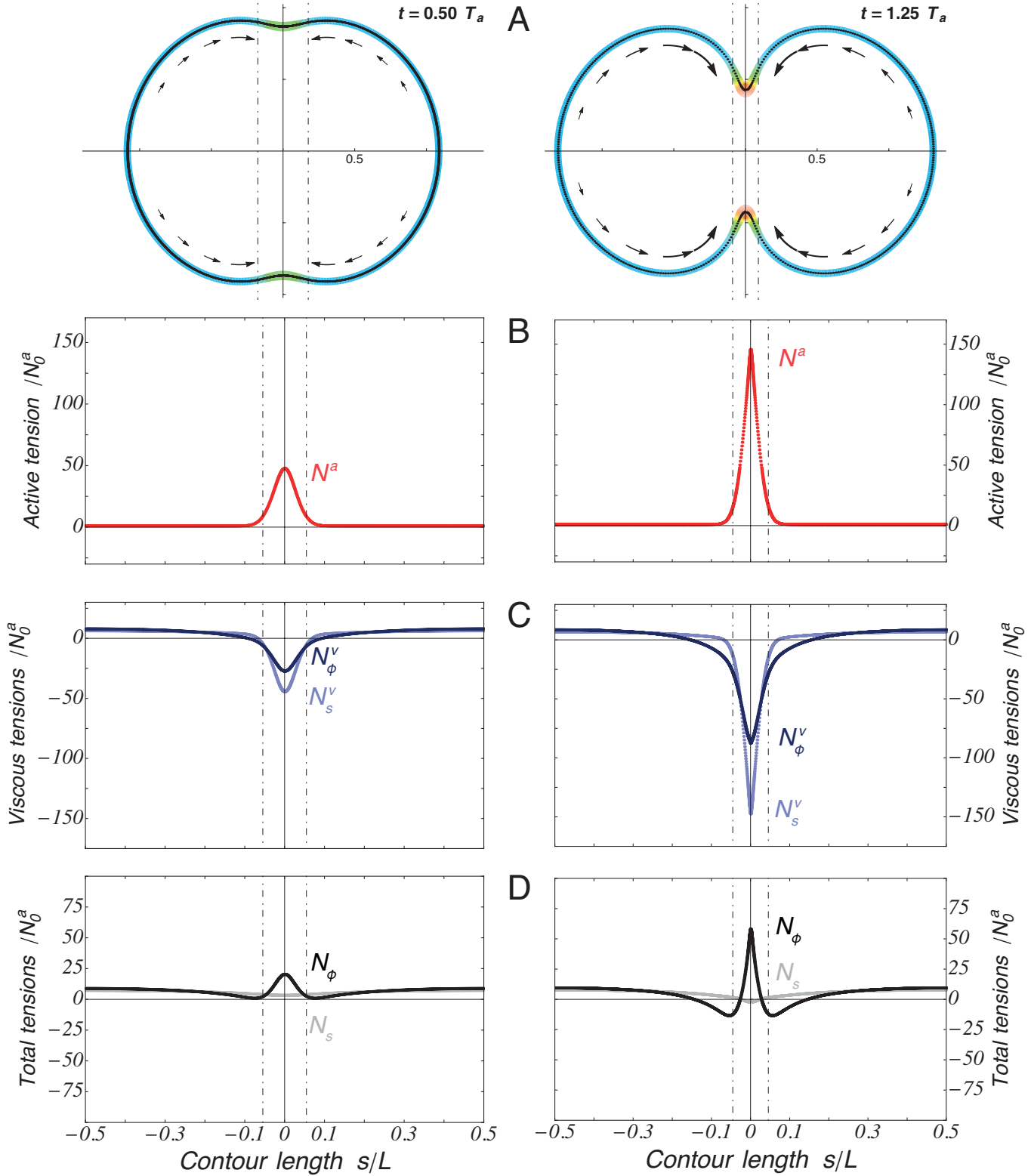


FIGURE S3: Cortical tensions: (A) Cell cortex shape and thickness at times $t = 0.5 T_a$ (left) and $t = 1.25 T_a$ (right). (B, C and D) Corresponding plots of, respectively, the active tension N^a , the viscous tensions N_s^v , N_ϕ^v and the total tensions N_s , N_ϕ in the membrane, rescaled by the basal active tension N_0^a . The active tension is isotropic in the axial and azimuthal directions whereas the viscous tensions are appreciably anisotropic near the furrow region, delimited by dot-dashed vertical lines. It leads to total membrane tensions that are globally anisotropic: the azimuthal tension is markedly greater than the axial tension in the furrow region leading to a furrow line tension that constricts the cell, whereas the regions bordering the furrow are more stretched in their axial direction leading to non-spherical shapes.

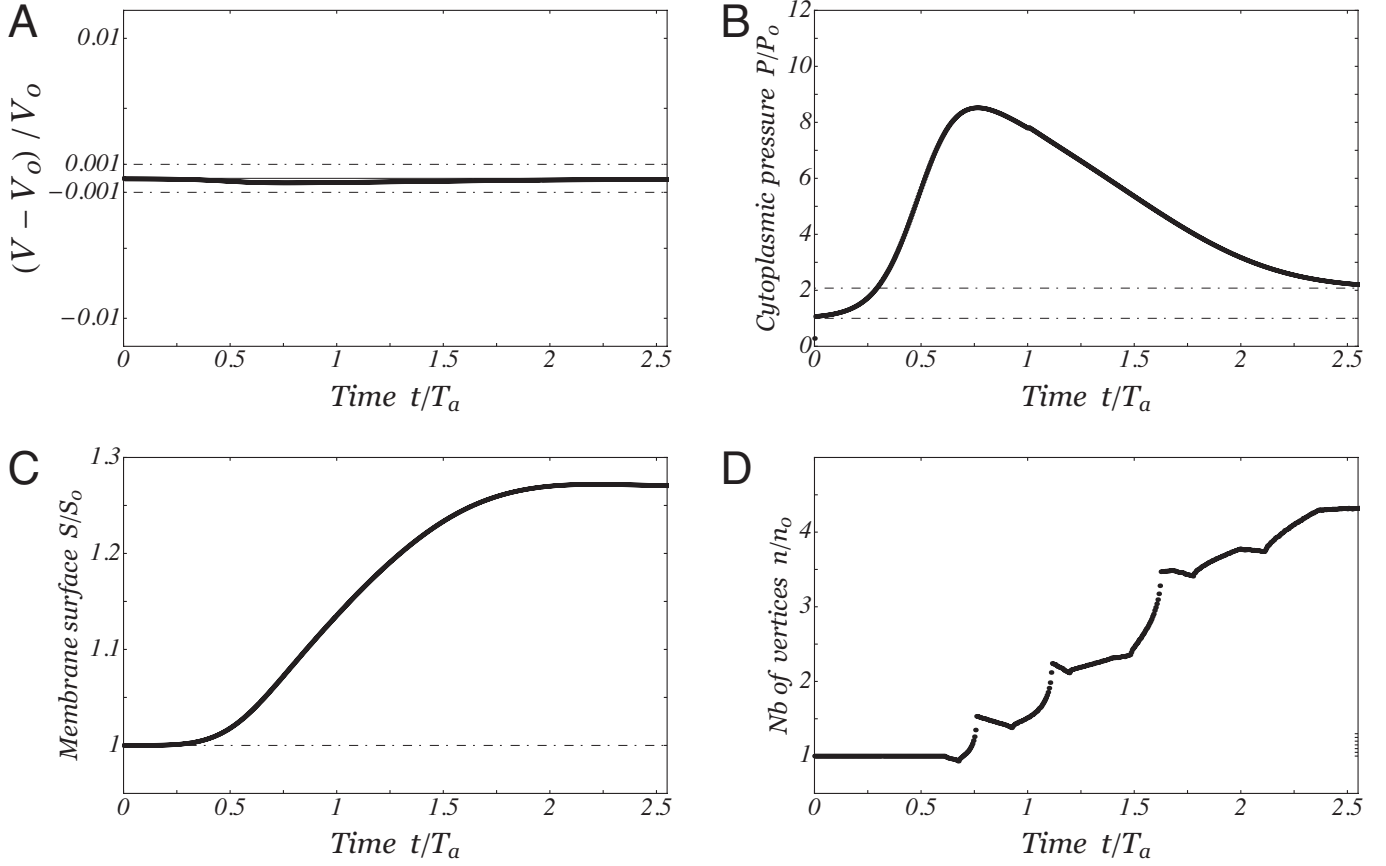


FIGURE S4: Cytoplasmic volume conservation and pressure, membrane surface and number of vertices for the first simulation (Fig. 1, Movies S1 and S5): (A) Plot of the cytoplasmic volume variation $(V - V_0)/V_0$ over time. We added two horizontal lines to show that the error is below 0.1%. (B) Cytoplasmic pressure P rescaled by the initial Laplace pressure $P_0 = 2N_0^a/R_0$. The cytoplasmic pressure increases rapidly during the transient phase and then decreases slowly toward a value roughly two times greater than the initial pressure. (C) Time evolution of the membrane surface S rescaled by the initial surface $S_0 = 4\pi R_0^2$. (D) Time evolution of the number of vertices n , rescaled by its initial value n_0 , as a result of the two adaptive remeshing procedures: refinement and coarsening.

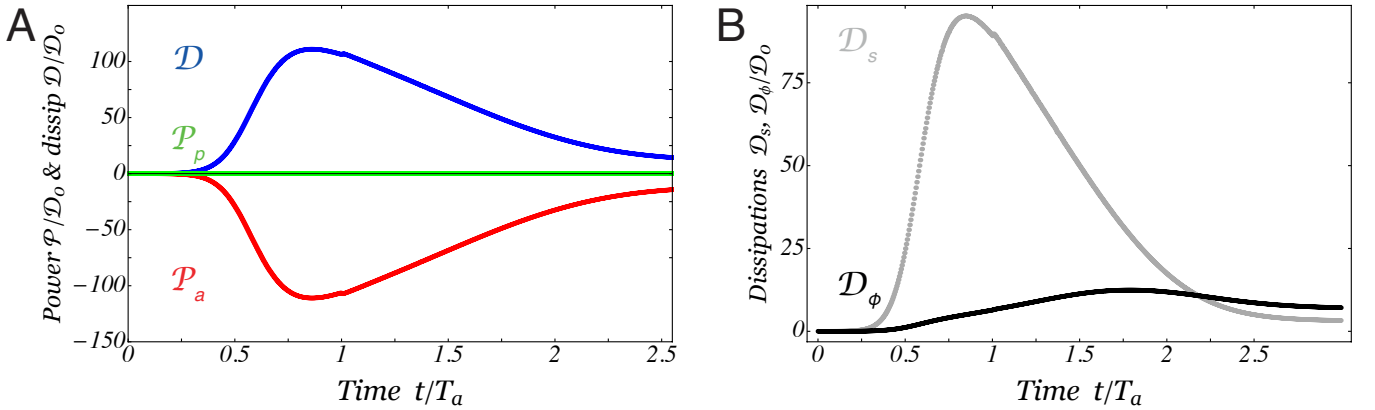


FIGURE S5: Active and dissipated power for the first simulation (Fig. 1, Movies S1 and S5): (A) Plot of the time evolution of the total dissipation \mathcal{D} , of the work of active forces \mathcal{P}_a in the membrane and of the work of cytoplasmic pressure \mathcal{P}_p rescaled by $\mathcal{D}_0 = 4\pi R_0^2 N_0^a / e_0 \eta$. We make the cytoplasm almost incompressible by assigning a high value of its bulk modulus $K = 250$. As a result it does not store any elastic energy and its work remains null. The work of active forces \mathcal{P}_a in the membrane is therefore fully dissipated by viscous effects \mathcal{D} . The work of active forces increases in the transient regime and then decreases almost linearly in time and finally relaxes exponentially towards a plateau above 0. We find again the successive phases of constriction described in Fig. 2 (Main text) and we confirm that maintaining a signal at equator sustains a cortical flow after constriction completion that maintains dissipation non-zero. (B) Plot of the time evolution of axial and azimuthal components \mathcal{D}_s and \mathcal{D}_ϕ of the viscous dissipation. The axial components reveals the dissipation due to cortical flows whereas the azimuthal component is essentially due to the furrow constriction. We observe that most of the dissipation comes from cortical flows occurring from the poles to the equator, except in the last phase of constriction for $t/T_a \gtrsim 2.5$ where the cortical flows decrease significantly.

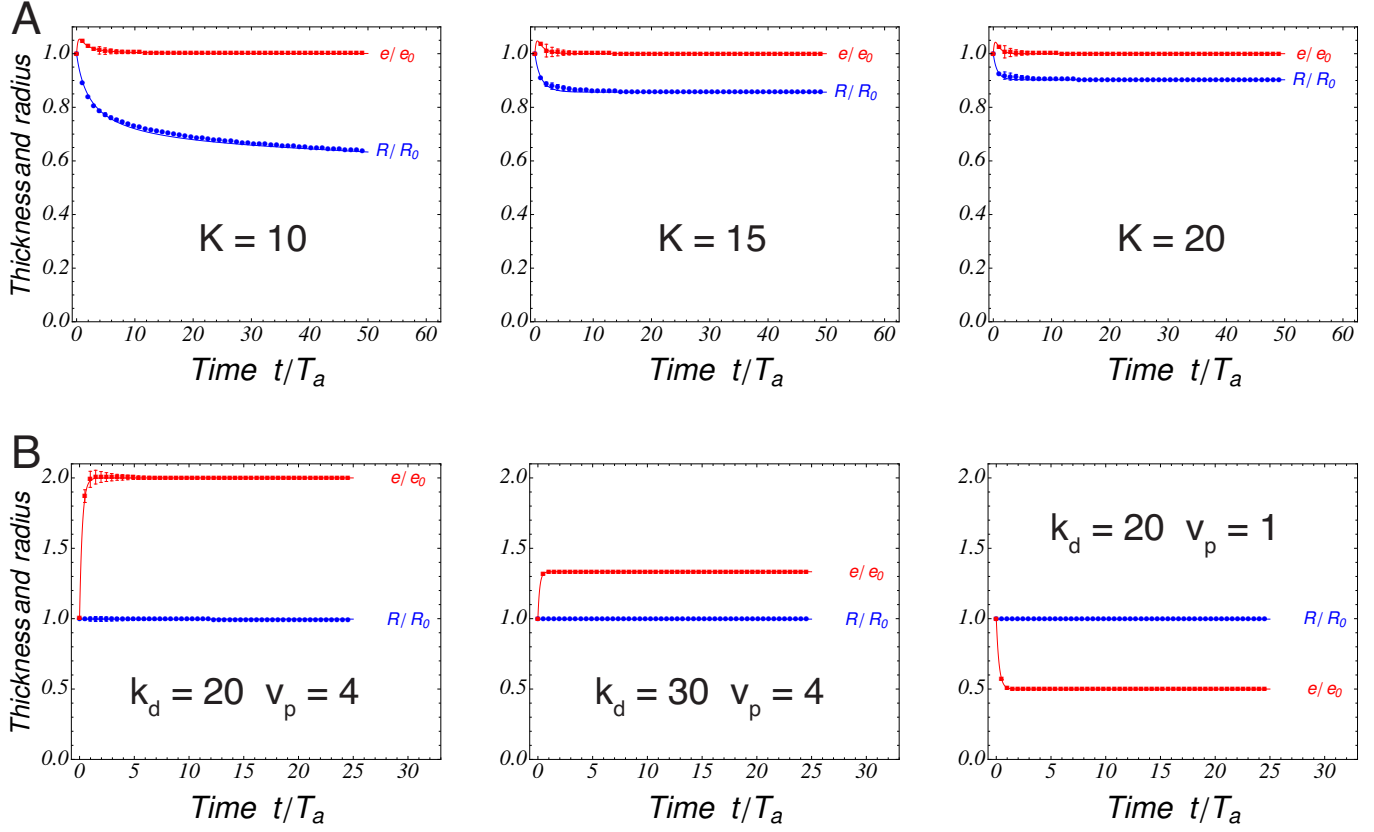
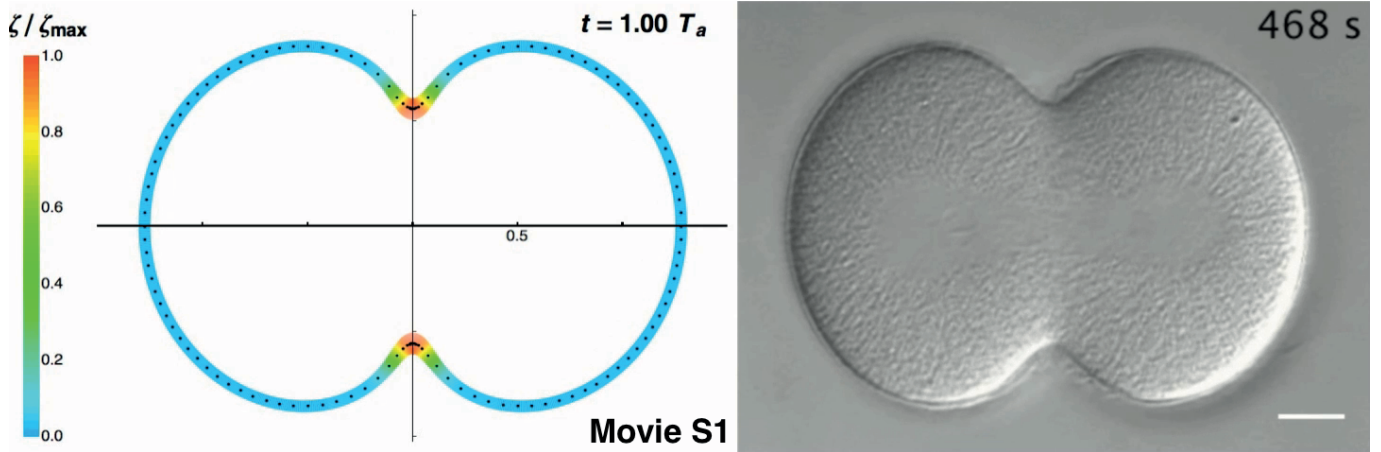
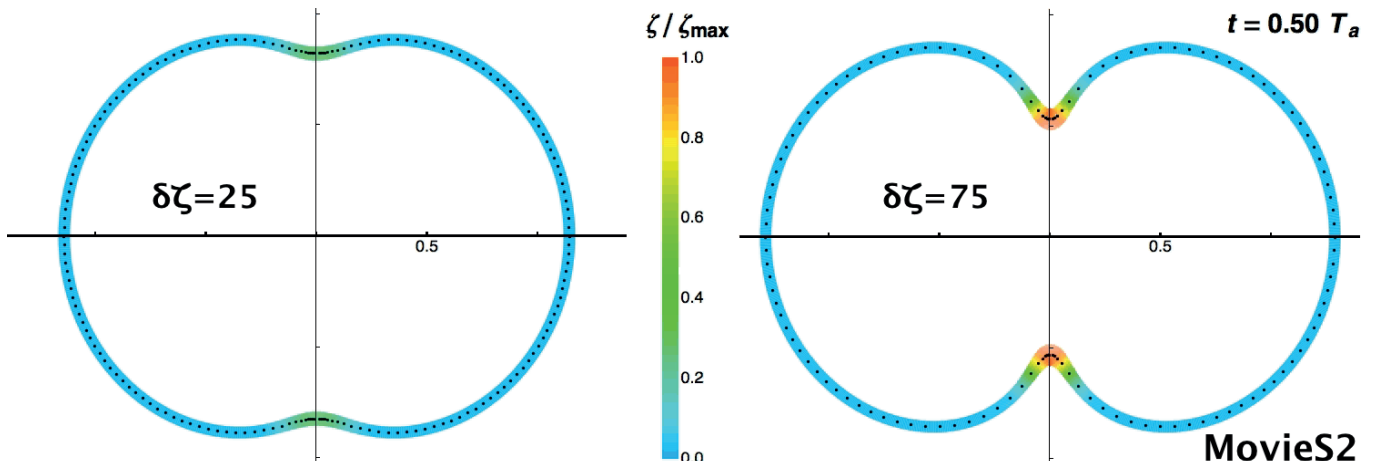


FIGURE S6: Code validation: spherical contraction under uniform active tension. Lines are solutions of the analytical equations for the cell radius R and membrane thickness e . Markers are solutions of the numerical model and error bars indicate maximum deviations along the membrane from the mean value. (A) Validation of the compressible cytoplasm implementation for three low values of the bulk modulus $K = 10, 15$ and 20 ($k_d = 40$ and $v_p = e_0 k_d = 0.1$). The cell radius contracts correctly under the effect of active tension and shows little longitudinal error. The amplitude of the contraction decreases when K increases as expected. The membrane thickness reaches rapidly its stationary value v_p/k_d . (B) Validation of the turnover implementation for three values of the depolymerization rate k_d and polymerization velocity v_p , so that the initial membrane thickness $e_0 = 0.1$ is different from v_p/k_d . A high value of the bulk modulus $K = 250$ maintains the cell radius R at its initial value R_0 to conserve cytoplasmic volume. In each case, the membrane thickness e reaches its stationary value v_p/k_d according to the analytical prediction and shows little error along the membrane.

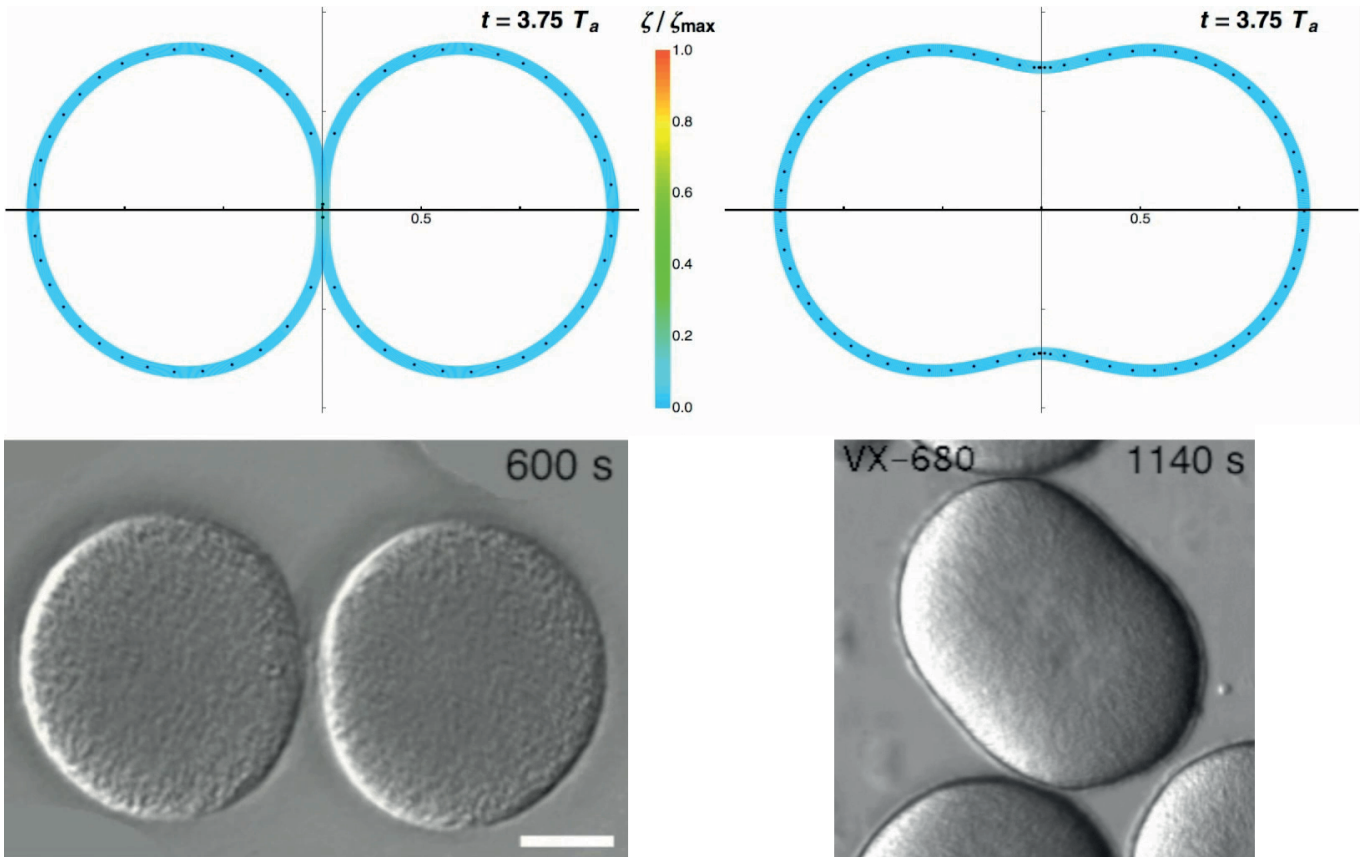
SUPPORTING MOVIES



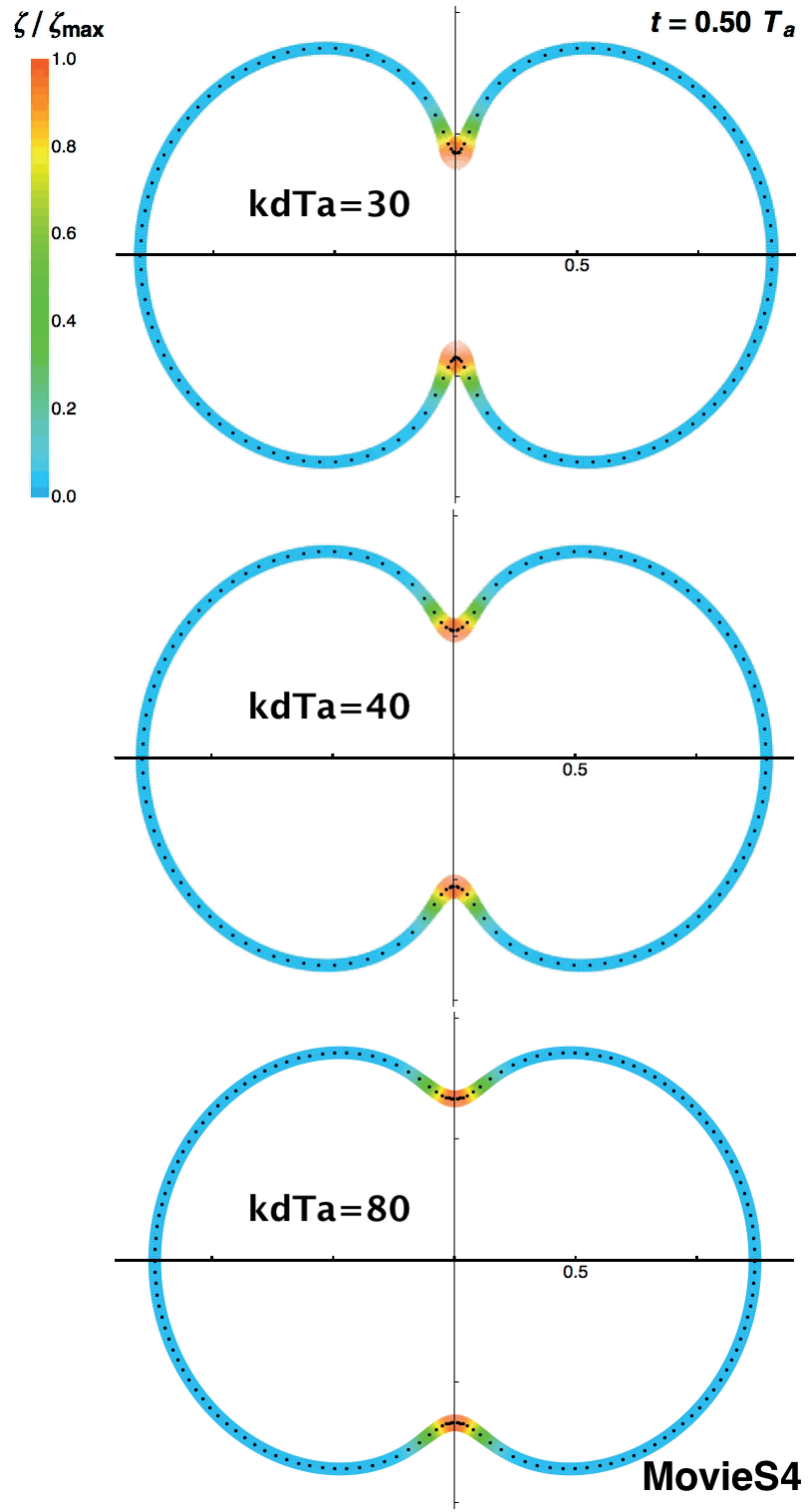
MOVIE S1: (Left) Dynamics of the cell shape and cortex thickness corresponding to Fig. 1 (Main text) in a section plane ($\mathbf{e}_z, \mathbf{e}_r$), in response to the rescaled activity signal ζ/ζ_{\max} , illustrated by the color shading. A few Lagrangian points are represented within the membrane to capture the cortical flows. (Right) DIC microscopy images of a sand-dollar zygote (dendraster) deprived of its hyaline layer and jelly coat under cytokinesis. The cell is not flattened and scale bar is $20\mu\text{m}$. (Credits: G. Von Dassow). Numerical and experimental movies have been synchronized by rescaling the active time scale to $T_a = 468\text{s}$.



MOVIE S2: Comparison of the cell shape and cortex thickness dynamics in a section plane ($\mathbf{e}_z, \mathbf{e}_r$) for the two equatorial signal amplitude $\delta\zeta^\infty = 25$, and $\delta\zeta^\infty = 75$, corresponding respectively to the furrow radius time evolutions ② and ⑤ in Fig. 3 B. A few Lagrangian points are represented within the membrane to capture the cortical flows

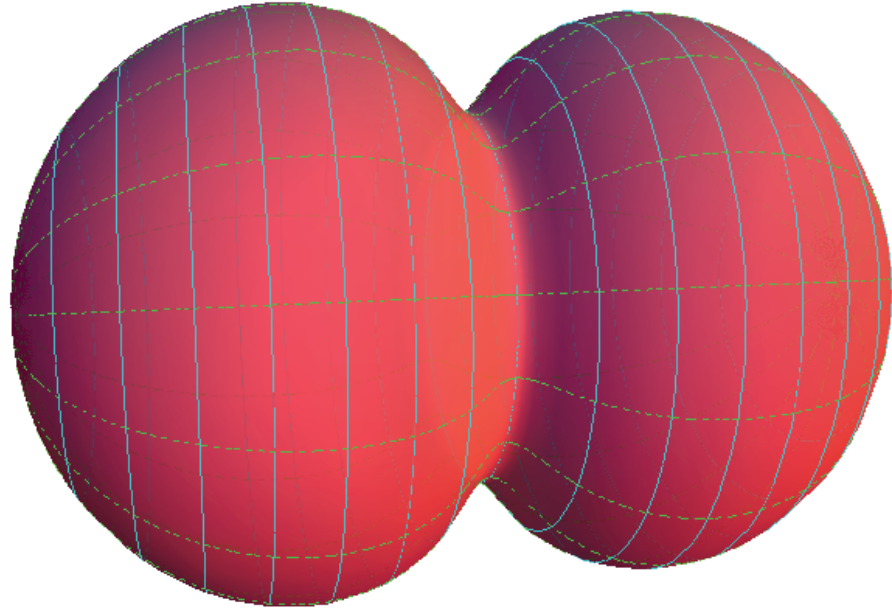


MOVIE S3: Illustration of the hysteretic behavior. **NUMERICS (Top)** Dynamics of the cell shape and cortex in a section plane ($\mathbf{e}_z, \mathbf{e}_r$) when the signal is decreased down to a value smaller than the threshold : (Top Left) after constriction completion or (Top Right) prematurely before the critical ingression radius $r_f \approx 0.6$ has been reached. **EXPERIMENTS (Bottom)** Qualitative comparison with the furrow constriction dynamics in sea-urchin eggs. (Bottom Left) Non-compressed *S. purpuratus* eggs in calcium-free artificial seawater and deprived of its hyaline layer (DIC microscopy, scale bar is $20\mu m$, credits: G. Von Dassow). The rounding up of cells at the end of furrow constriction (without cell adhesion) may be attributed to a decrease of the equatorial signal according to numerical results above. The divided state remains mechanically stable. (Bottom Right) *L. pictus* egg deprived of its enveloppe and cultured in natural seawater with 50 mM VX-680 (24) (DIC microscopy, credits: C. Bradley Shuster). The regression of the furrow, which leads to a binucleated cell, may be attributed to a premature decrease of equatorial contracility according to numerical results above.



MOVIE S4: Comparison of the cell shape and cortex thickness dynamics in a section plane (e_z, e_r) for the three turnover rates $k_d T_a = 30$, $k_d T_a = 40$ and $k_d T_a = 80$ at fixed equatorial activity amplitude $\delta\zeta^\infty = 75$, corresponding respectively to the furrow radius time evolutions ①, ② and ③ in Fig. 4 (Main text). A few Lagrangian points are represented within the membrane to capture the cortical flows

1.00 Ta



Movie S5

MOVIE S5: Dynamics of the cell shape in 3 dimensions, corresponding to Fig. 1 (Main text) and Movie S1.